

POLITECNICO DI TORINO

Corso di Laurea Magistrale
in Ingegneria Aerospaziale e Astronautica

Tesi di Laurea Magistrale

**Modeling and Control of a Space Drone
for Mars Exploration Mission**



Relatore:

Elisa Capello

Correlatore:

Mauro Mancini

Candidato:

Giovanni Piccione

Anno Accademico 2020/2021

Abstract

The possibility of exploring new planets and the continuous need to enrich our knowledge of the universe has led to the development of different space systems capable of collecting data and transmitting them to the Earth through space. Different mission scenarios should be considered, from Earth Observation to the exploration of deep space. In recent years, however, the ever growing interest, both by large space companies and by private ones, for the "Red Planet" has led many scholars to search for solutions to face the tough challenge of exploration in a hostile environment and very different from the terrestrial one. Among the various problems, landing is of particular importance: in fact, it should be considered that only half of the landing attempts were successful. The most recent of these missions is *Perseverance*, a martian rover that has succeeded in this arduous scope. Among its objectives, this mission also has a very delicate technological demonstration: to perform a flight through the *Ingenuity* drone that traveled and landed together with the rover. In fact, these systems can explore larger surfaces regardless of the topography, allowing a wider view of the surrounding environment.

Moved by the same purposes, in this work, the results of a feasibility study of a similar mission are investigated by focusing on the precision landing and soil exploration phase. The analysis has as its starting point the selection of different configurations able to perform the mission. Later, the mathematical models of the equations of motion on MatLab/Simulink, the geometry and physical structure of the systems are developed. These first outputs are essential to understand the actual feasibility of the project, especially in terms of weights and dimensions. The results led us to choose two systems: a parafoil equipped with a controller to perform a precision landing and a quadcopter drone to perform flight tests.

This work presents a dynamic model (a 6 Degree-of-Freedom (DoF) system) of the drone system that must be able to perform various maneuvers. It takes a desired path as input and follows it within a certain range of error. The scope of this thesis is to model a space drone, able to accomplish the desired missions, even in Mars environment. In this environment, wind effect and low density cannot be neglected. Moreover, a key feature of the using space drone is the mapping and ability to handle payloads for collecting data. Then, by modeling the Martian environment, it is possible to run software simulations, performing maneuvers and evaluating

their accuracy in order to understand system performance. This is essential for the choice of the Guidance and Control Laws to be applied for autonomous operations, necessary given the latency times in the communications caused by the great distance between the two planets.

Acknowledgment

I would like to thank my advisor Professor Elisa Capello and co-advisor Mauro Mancini who have guided me through this project showing great professionalism, dedication and love for their work. A few lines would not be enough to describe the enthusiasm, knowledge and passion they have transmitted to me. A special thanks goes to my colleague Alessandro Mercurio who has conducted this work with me. Moreover, i would like to thank my family, my girlfriend and my friends for supporting and allowing me to achieve this goal.

Contents

List of Figures	vi
List of Tables	ix
Acronyms and Abbreviations	x
1 Introduction	1
1.1 Research objectives	1
1.2 Possible target planets	3
1.2.1 Venus	3
1.2.2 Titan	4
1.2.3 Mars	5
1.3 Mars aerobots background	8
1.3.1 Fixed-wing	8
1.3.2 Rotary-wings	9
1.3.3 LTA vehicles	11
1.3.4 Flapping-wings	13
2 Mathematical models	14
2.1 Mars environment	14
2.2 Reference frame	17
2.2.1 Mars Inertial Frame	17
2.2.2 Body Frame	17
2.3 Gravity model	19

2.4	Atmosphere model	20
2.5	Wind model	21
2.6	Drone’s models	24
2.6.1	Kinematics model	26
2.6.2	Dynamics model	27
2.7	Parafoil’s models	29
2.7.1	Kinematics model	30
2.7.2	Dynamics model	31
3	Drone’s dynamics simulator	37
3.1	Drone configuration	38
3.1.1	Propellers	38
3.1.2	Electric motors and batteries	42
3.1.3	Total mass and inertia tensor	44
3.1.4	Iterative loop	47
3.2	Guidance and Control	49
3.2.1	Guidance algorithm	49
3.2.2	Control design	51
3.3	Actuators	57
4	Test and results	58
4.1	Hovering	58
4.2	Simple translation	63
4.3	Square maneuver	67
5	Conclusions & Open points	69
	References	71

List of Figures

1.1	Profile of Venus’s atmosphere	3
1.2	Rotary wing decelerator for Venus probe by Young	4
1.3	Solar Venus drone designed by Landis	4
1.4	Titan’s atmosphere profile	5
1.5	Titan’s drone concepts: Dragonfly and Montgolfiere baloon flagship	5
1.6	average Mars atmosphere parameters versus altitude	6
1.7	ARES-2 configurations for Mars exploration	9
1.8	Representation of Mars Helicopter Ingenuity on the surface of Mars	11
1.9	A schematic view of a flying wing with vertical and horizontal flight modes	11
1.10	View of designed and manufactured Balloon Guidance System for Mars exploration	12
1.11	Parafoil model	12
1.12	View of Entomompter designed by Colozza for Mars exploration	13
2.1	Illustration of Martian Solar Longitude Diagram	14
2.2	A Comparison of Rotor Thrust Generated on Earth and Mars	16
2.3	Mars Inertial Reference System	17
2.4	Body Reference Frame for drone and parafoil system	18
2.5	Global Gravity Map of Mars	19
2.6	Average wind in Mars during winter at 10m altitude	21
2.7	Average wind with Bias of 10%	22
2.8	Average wind with Bias of 10% and Noise	23
2.9	Wind model operating diagram	23

2.10	Example of Bicopter	24
2.11	Example of Tricopter "Y" shaped	24
2.12	Example of Quadcopter "+" and "x" shaped	25
2.13	The ram-air parachute	29
2.14	Free body configuration of the parafoil-payload system.	30
2.15	Volumetric Representation of Apparent Masses and Moments	35
3.1	Drone's simulator	37
3.2	Values of C_t and C_q as the angular velocity varies	39
3.3	Mass as a function of radius for drone propellers and model helicopter propellers	41
3.4	Drone inertia model outline	45
3.5	Drone's mass calculation flowchart	47
3.6	Guidance algorithm structure	49
3.7	Principal Guidance algorithm's parameters	50
3.8	Counter and square waves generator	51
3.9	Controller typical structure	52
3.10	PID controller basical structure	53
3.11	Cascade controller structure	54
3.12	Position controller structure	55
3.13	θ and ϕ controller	55
3.14	ψ controller	56
3.15	Attitude controller	57
4.1	Evolution of position in Hovering condition	59
4.2	Evolution of position in Hovering condition with wind	59
4.3	Error caused by wind during Hovering maneuver	60
4.4	Effect of errors on command torque	61
4.5	Attitude angles during Hovering maneuver	62
4.6	Trajectory of the drone in Simple translation maneuver	63
4.7	Evolution of position in Simple translation maneuver	64
4.8	Evolution of velocities in Simple translation maneuver	64
4.9	Command torque during Simple Translation maneuver	65

4.10	Position errors caused by wind in Simple Translation maneuver	66
4.11	Attitude errors caused by wind in Simple Translation maneuver	66
4.12	Trajectory of the drone in Square maneuver	67
4.13	Output of Square pattern	68
4.14	Maneuver failure in windy condition	68

List of Tables

1.1	Comparison between Earth and Mars	6
1.2	ARES-2 Mars drone parameters	9
1.3	Merits and Limitations of Large and Small Mars Rotorcrafts	10
1.4	Mars Ingenuity features	10
2.1	Comparison of Relevant Earth and Mars Parameters	15
2.2	Apparent masses and inertias comparison between Earth and Mars for a parafoil of 13 m ² wing surface	36
3.1	Helicopter's propellers data	39
3.2	Drone's propellers data	40
3.3	Selected propeller's data	41
3.4	DJI E305 peculiarity	42
3.5	lithium polymer battery (Li-Po S4) peculiarity	44
3.6	Drone configuration parameters	48

Acronyms and Abbreviations

\bar{R}	Specific gas constant
γ	Heat capacity ratio
μ	Dynamic viscosity
ν	Kinematic viscosity
ω	Angular velocity
ρ	Density
ξ	Battery's specific energy
C	Capacity
g	Gravitational acceleration
L	Reference length for Reynolds number
m_b	Battery's mass
P_e	Electrical power
P_m	Mechanical power
P_w	Maximum engine power
r_c	Discharge rate
Re	Reynolds number
T	Thrust
$^{\circ}\text{C}$	Celsius
J	Joule
K	Kelvin
kg	Kilogram
m	Metre
Pa	Pascal
s	Second
V	Voltage
W	Watt
Wh	Watt-hour
L	Distance between two adjacent rotors

A	Rotor Area
AR	Aspect Ratio
BET	Blade Elementary Theory
C_L	Lift coefficient
C_Q	Torque Coefficient
C_T	Thrust Coefficient
CCW	Counter Clockwise
CM	Centre of Mass
COTS	consumer off the shelf
CW	Clockwise
DoD	Depth of Discharge
DoF	Degrees of Freedom
E	Battery's energy
ESC	Electronic Speed Controller
I	Current
JPL	Jet Propulsion Laboratory
L	Lift
LTA	Lighter-than-atmosphere
MARV	Martian Autonomous Rotary-wing Vehicle
MAV	Micro Air Vehicles
MI	Martian Reference system
NASA	National Aeronautics and Space Administration
NED	North-East-Down Reference System
ODE	Ordinary differential equation
p	Pressure
PADS	Precise aerial delivery system
Q	Torque
R	Gas constant
S	Surface area
T	Temperature
UAV	Unmanned Aerial Vehicles
v	Velocity
w.r.t	with respect to

1. Introduction

1.1 Research objectives

Thanks to technological development in the last decades, the presence of space agencies in space increased. Nowadays it's possible to explore space bodies with different approaches, which can be classified into seven groups including Earth-based observations, airborne and orbital telescopes, probes and fly-by spacecraft, orbiters, landers, rovers, and sample return [1]. The attention of space agencies has particularly focused on our solar system, which has four inner planets, four gas giant planets and 66 moons in total. Of these moons, one has atmosphere, 16 have water, ice or ocean, and 5 with both atmosphere and water or ice [1]. The presence of atmosphere on some planets and moons have inspired a new approach to space bodies exploration: aerobots. These new concept vehicles have the ability to explore greater ranges than rovers or landers. Also, these flying vehicles due to their proximity to the planet's surface could provide more high resolution information compared to the orbiters [1]. Aerobots include fixed, rotary and flapping wings drones, aerial balloons and Lighter-Than-Atmosphere vehicles (LTA). They can be applied to explore, characterize, and determine potential human landing sites [1] and help future astronauts in the exploration of a planet. Another application of some of these vehicles is to perform an autonomous precise landing of rovers or landers, which are also known as Precise Aerial Delivery Systems (PADS).

However, not all the planets and moons of our solar system containing an atmosphere are good candidates for aerobots: some of them have a too thin atmosphere, some don't have a surface and some have too much strong winds. In practice only three of them are appropriate: Mars, Venus and Titan.

In the last decades Mars has raised more and more interest in the scientific community and in various space agencies. Aerobots, in particular Unmanned Aerial Vehicles (UAVs), are increasingly more considered as valuable platforms for planetary exploration. In this thesis two different types of UAVs are presented for a mission on Mars: a quadcopter drone and a parafoil system. These UAVs have very different characteristics and purposes. The drone is an optimal platform for the exploration of hazardous sights for common rovers, like caves or deep craters. While the parafoil system is a PADS that can be used to perform precise rover landings.

The aim of this thesis is to study and evaluate the feasibility of these two aerobots for a mission on Mars, with a focus on the drone system. The particularity of this latter type of mission is that it will be carried out for the first time this year in the first week of April thanks to the Ingenuity drone [2]. Prior to this, several studies are carried out, some of which are supported

by specific indoor tests like *The Martian Autonomous Rotary-wing Vehicle* (MARV) [3]. For this reason, in this work similar studies are conducted to develop an equivalent design that can perform the flight. It takes experimental data as its starting point and includes a re-adaptation of geometries already used in the terrestrial environment. Then, using Matlab-Simulink software, the dynamic and kinematic equations are considered and designed, to reproduce the motion of the system in a simulated martian environment. A simplified dynamics model is used to represent the quadcopter, which neglects the aerodynamic drag acting on the body. The ability to drive autonomously is a key point for the success of the mission, so control techniques are tested. In particular, a cascade controller capable of controlling the elements of the vector states step by step, is selected [4]. By reading the status of the system from the sensors and converting the data into the appropriate reference systems, this series of Proportional, Integrative and Derivative controllers (PID) can guide the drone to predefined points with tolerable margins of error. Adding the delays due to the sensors and motors actuation times to the equations of motion and control described above, a 6 DoF dynamic simulator is obtained to analyse the trajectories and behaviour of the aerobot and determine the feasibility of the mission. The same maneuvers are tested both with and without wind disturbances, since it can affect the flight; it is modeled as an oscillation around an average value taken from the Mars Climate Database [5].

1.2 Possible target planets

There is evidence that many space bodies in our Solar System have atmosphere. The atmospheric characteristics of these solar bodies usually are different regarding their size, distance from the Sun, gravity, the type of gases, etc. [1]. The majority have an extremely thin atmosphere, like Earth's Moon, Io, Ganymede, Europa, Callisto and other natural satellites. Uranus, Saturn and Jupiter don't have a solid surface were to land and a dense atmosphere with strong winds. Pluto and Neptune have extreme atmospheric conditions as well. Only three solar bodies have good atmospheric conditions for flying vehicles: Venus, Saturn's satellite Titan and Mars. These bodies are good candidates, but have very different features between them, which define different design requirements.

1.2.1 Venus

Venus is an interesting target for scientific community: knowing its evolution could help understand how Earth-like planets evolve, although it's not suitable for human life.

Venus is extremely hot and has an atmospheric pressure on the surface 92 times higher than Earth atmosphere. The atmosphere mostly consist of carbon dioxide, a greenhouse gas, for this reason the mean surface temperature is 735 K. Another feature of the planet are the strong winds, with speeds that reach up to 85 m/s.

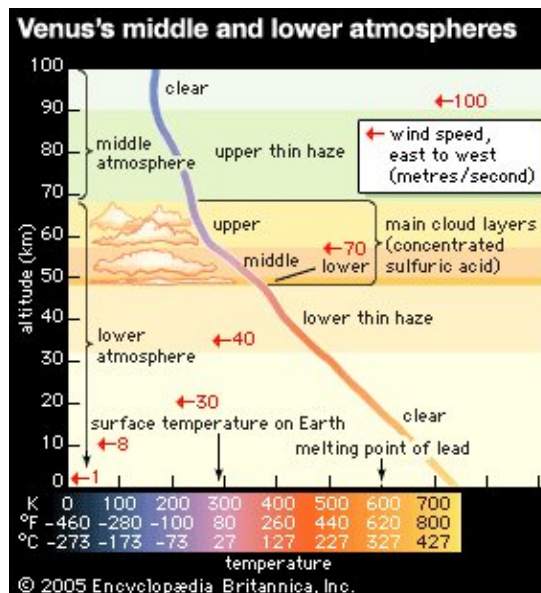


Figure 1.1: profile of Venus's atmosphere, Image credits: Encyclopædia Britannica

The troposphere begins at the surface and extends up to an altitude of 65 km. Therefore, in Venus, from an altitude of approximately 45 km, where the pressure is 2 bars, the temperature is 80 °C, and wind speed is about 45 m/s, to approximately 60 km, where the pressure is 0.2 bars, the temperature is -35 °C, and wind speed is 100 m/s [1]. In this region it's possible to design a drone capable of flying on Venus, due to the Earth-like atmospheric pressure. Furthermore Venus has a higher value of solar intensity compared to Earth. For this reason some balloons, airships and solar drones were designed in the past years, with the intention of remaining over 60 km of altitude for a long period of time. Other studies proposed to use rotorcrafts for atmospheric entry probe deceleration, due to the higher values of atmospheric density, which allows the use of small rotors for this purpose.

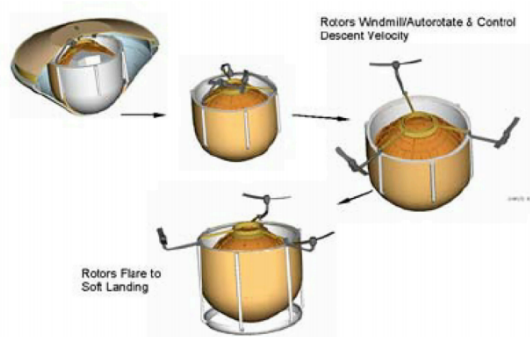


Figure 1.2: rotary wing decelerator for Venus probe by Young [1]

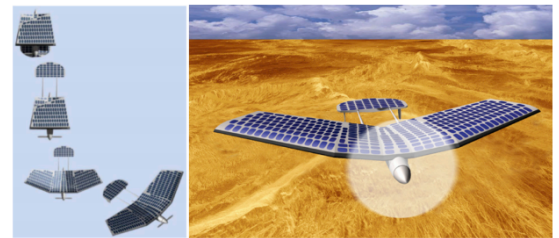


Figure 1.3: Solar Venus drone designed by Landis [1]

1.2.2 Titan

Saturn's moon Titan is likely the richest laboratory in the solar system for studying prebiotic chemistry, which makes studying its chemistry from the atmosphere to the surface one of the most important objectives in planetary science. Studying Titan's organic chemistry requires landing to sample and analyze fluids, dissolved species, and sediments from Titan's seas, lakes, tidal pools, or shorelines [6]. It is the second largest satellite in the solar system and its atmosphere consist of nitrogen (98.4%), methane (1.6%) and other gases. Therefore, Titan's atmosphere is denser than Earth's atmosphere, with a surface pressure of 147 kPa [1] and a mean surface temperature of 94 K, and 60 m/s winds speed.

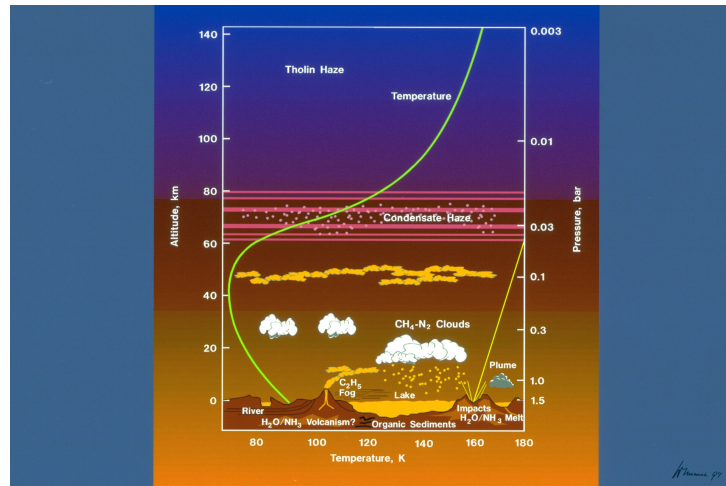


Figure 1.4: Titan's atmosphere profile, Image credits: ESA

In the last years different UAVs were proposed for the exploration of Titan: a balloon concept and a rotorcraft drone. These UAVs enable the study of large areas of the surface. Another LTA vehicle could be used on Titan: a parafoil system. Landing dispersions with existing technology are hundreds of kilometers wide [6], therefore reduce this dispersion is a big issue. The parafoil system, thanks to its controllability and lightness, its a promising concept to solve this problem; for Titan landings, but also for Mars.



Figure 1.5: Titan's drone concepts: Dragonfly and Montgolfiere balloon flagship [1]

1.2.3 Mars

The scientific community has supposed that Earth and Mars have been relatively similar worlds in the past. For this reason the red planet has aroused more and more attraction from space agencies, which have visited it several times in the past 50 years with rovers, probes, orbiters and landers. As said before, in recent years the idea of exploring Mars with aerobots has attracted lots of attention, for this reason the Red planet is the chosen target for our study.

Table 1.1: Comparison between Earth and Mars

	Earth	Mars
mass (10^{24} kg)	5.97	0.64
volume (10^{10} km ³)	108.3	16.3
average distance from Sun (10^6 km)	149	228

Mars atmosphere is very thin and dusty and mainly composed of carbon dioxide [1] (96%) and some traces of argon, nitrogen, water and oxygen. The average surface pressure is between 0.4-0.87 kPa, which is similar to Earth's atmospheric pressure at 30.5 km altitude. Mars has four seasons like Earth and temperatures vary from -140°C in winter, to 20°C in summer, while winds speed can vary from 2-7 m/s during summer to 17-30 m/s in a dust storm as reported on [7].

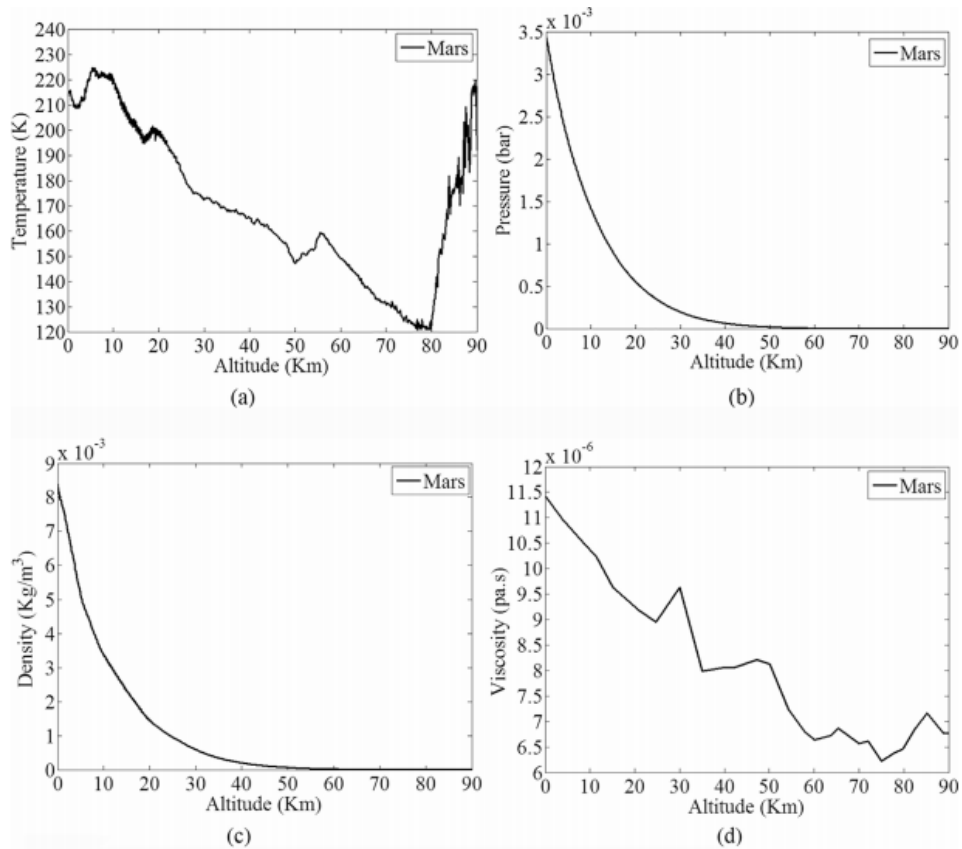


Figure 1.6: average (a)temperature, (b)pressure, (c)density, (d)viscosity of Mars atmosphere versus altitude [1]

Flying on Mars is an immense challenge: the Reynolds number of drones are on scale of 10^5 , while on Earth are on scale of 10^6 , due to its lower atmospheric density. The speed of sound is 20% lower than on our planet, so it's easier to reach transonic velocities and generate

destructive shock waves on the body, wing or propellers of the aerobot. Moreover, due to low percentage of O_2 in the martian atmosphere, conventional combustion propulsion systems, such as oxygen-breathing motors and engines cannot be implemented on martian drones. Therefore, martian drones propulsion systems would rely on electrical or chemical systems [1]. These limitations have many implications on the design of a martian flying vehicle. In the following section some types of Mars flying vehicle concepts are presented.

1.3 Mars aerobots background

As reported before, aerobots can fulfil several exploration goals: exploring rough terrain for rovers and landers, offer high resolution images of landscape, soil composition analysis of large areas with gamma ray spectrometers or other techniques, magnetism analysis around geological features, offer a more precise landing of probes.

The design of a martian aerobot depends both on the atmospheric features of the planet and the mission objectives. Therefore very different aerobots concepts have been designed, which can be gathered in four categories: fixed wing, rotary wing, LTA vehicles and flapping wings.

1.3.1 Fixed-wing

Due to the low density of the martian atmosphere and the low Reynolds number, fixed-wing drones should fly at very high speed, on the order of 0.6 Mach, and have a large wing area to generate the required lift force. If the drone is powered with propellers, these should be large and could not rotate too fast, for the same reasons. For fixed wing drones, the required lift coefficients to operate on Mars and Earth can be compared as follows:

$$\frac{C_{LM}}{C_{LE}} = \frac{W_M \rho_E S_E V_E^2}{W_E \rho_M S_M V_M^2} \quad (1.1)$$

Where W , ρ , S and V represent the weight, density, wing area and flight speed, respectively on Mars with index M , and Earth with index E [1]. Since Mars gravity is 1/3 of Earth's gravity, $W_M/W_E \simeq 1/3$. In addition it's known that $\rho_E/\rho_M \simeq 60$. Applying these ratios in equation 1.1, one obtains:

$$\frac{C_{LM}}{C_{LE}} \approx 20 \frac{S_E V_E^2}{S_M V_M^2} \quad (1.2)$$

In equation 1.2 it can be seen that drones in Mars environment need a lift coefficient 20 times greater than on Earth, for the same given wing area and flight speed. Otherwise it could be increased the wing area or the flight speed to increase the lifting force.

Existing airfoils provide maximum C_L values of ~ 2 , therefore new airfoil shapes should be designed for flying on Mars. Drones with large wing area might need to utilize a folding scheme to fit inside the aeroshell used for the planetary entry phase. Moreover, high flight speeds causes some difficulties and complexities for landing, take-off and power requirements. Thus, the designed drone for Mars exploration can perform a single cruise flight [1].

An example of Mars fixed-wing drone is the *ARES-2* project proposed by NASA Langley Research center and JPL. *ARES-2* science objectives required completion of a 500-km pre-planned science survey from a vantage point 1-2 km above the surface terrain.

During this traverse, unique measurements of the Mars atmosphere, surface and the interior would be obtained using magnetometers, a mass spectrometer, a point spectrometer, and imaging cameras [8]. The airplane was designed with a folding scheme to fit inside the aeroshell and deploy at an altitude between 2-3 km.

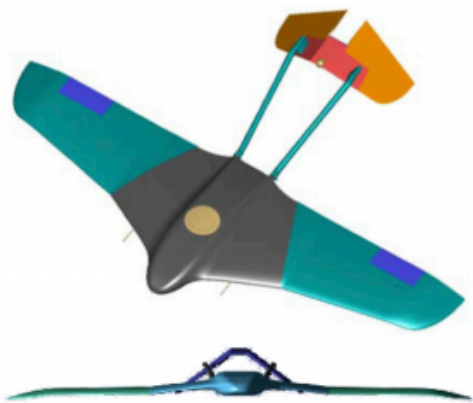


Figure 1.7: ARES-2 configurations for Mars exploration [1]

Table 1.2: ARES-2 Mars drone parameters

ARES-2 parameters	
wingspan	6.25 m
wing area	7 m ²
overall length	4.4 m
overall height	0.7 m
reference chord	1.25 m
aspect ratio	5.58
wing sweep	30°/13°
cruise speed	145 m/s
mass	175 kg

As reported in Table 1.2 *ARES-2* has a high cruise speed and large wing area, thus a soft landing in a short range is quite impossible for this type of vehicle. Since the objective to perform a precise autonomous landing for a rover, another aerobot has been selected, lighter and easier to store inside an aeroshell: the parafoil system.

1.3.2 Rotary-wings

Rotary wing drones can perform vertical take-off, landing, and hovering flight in different solar bodies [1], enables remote-site sample return to landers with precision placement, have greater range of exploration than rovers. For these reasons these platforms are considered the most suitable configurations for Mars exploration, although drone's propellers have low performance in the thin Mars atmosphere.

Limitations on the propellers of these types of drones are various: the rotational speed should be lower and the radius higher than on Earth, due to the lower atmospheric density and lower speed of sound. Moreover the low temperatures on the planet are a problem for electrical driven motors: battery performance decrease considerably at low temperatures.

Rotorcrafts can have different capabilities and advantages according to their size, as reported in the Table 1.3.

Table 1.3: Merits and Limitations of Large and Small Mars Rotorcrafts [9]

Small Rotorcraft	Large Rotorcraft
<i>Capabilities</i>	<i>Capabilities</i>
<ul style="list-style-type: none"> • Perform efficient short- and mid-range “low and slow” aerial surveys • Take off and land at remote unprepared sites • Drop small probes and sensors and/or acquire small samples of soil and rocks • Act as advance scouts for human explorers or large robotic rovers • Act as, or transport and install, telecom and data relays • Perform high-risk and/or “expendable” tasks 	<ul style="list-style-type: none"> • Can carry more sophisticated instrument packages than smaller platforms • Greater range than smaller platforms • Medium size high-value payloads point to point • Possibly act as a short to mid-range “manned” transport platform
<i>Advantages</i>	<i>Advantages</i>
<ul style="list-style-type: none"> • One or many Mars rotorcraft working together in concert • Almost de facto robotic symbiosis of small rotorcraft working with other robotic/automated systems 	<ul style="list-style-type: none"> • In general, at most, one or two larger rotorcraft work together to perform tasks • Larger rotorcraft would be used for campaigns leading up to and including human exploration
<i>Disadvantages</i>	<i>Disadvantages</i>
<ul style="list-style-type: none"> • Range limited for small platforms to an operational radius of less than 50km • Relatively high energy expenditure for a robotic asset, but not too high as compared to other equipment required for human exploration of Mars 	<ul style="list-style-type: none"> • Range for larger vehicles increases to an operational range of a couple hundred kilometers • Larger rotorcraft consume large quantities of energy; however, compared to energy requirements for ISRU for return-to-Earth propellant, or human habitat and base camp power needs, then energy levels required are not too excessive

An example of small Mars rotorcraft is NASA’s *Mars helicopter Ingenuity*, landed in these months on Mars along with *Perseverance* rover. This drone is a coaxial autonomous helicopter, and the project is solely a demonstration of technology; it is not designed to support the *Mars 2020/Perseverance* mission [2]. As one can see in Table 1.4, the drone’s weight is quite low and the rotor system span is high.

Although this configuration allows to have a compact and light drone, in this thesis a different architecture is presented: a quadcopter. Such configuration is equally light, but less compact and has the advantage of having a simpler dynamics model, that makes this architecture the best for a preliminary design.

Table 1.4: Mars Ingenuity features, reported on [2]

Ingenuity features	
Height	0.49 m
Rotor system span	1.2 m
Weight	1.8 kg
energy	Solar-powered and recharges on its own
rotors rotational velocity	2400 rpm



Figure 1.8: Representation of Mars Helicopter Ingenuity on the surface of Mars [2]

Others rotary-wing drones are tilt-rotors, tilt-wing and tilt-body drones, which can be considered as the future of space drones configurations. Applying a rotating propulsion system on a flying wing can provide all the advantages of a fixed wing with forward flight and a rotary wing drone with hovering capabilities [1]. The disadvantages of these drones is that with even relatively small "gross weight" masses will likely require astronaut assembly, because of the large wing surfaces entailed by these vehicles [9].

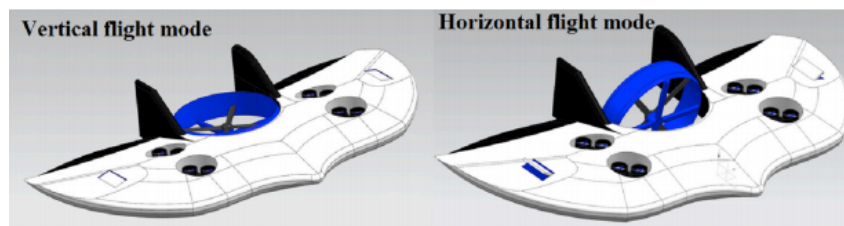


Figure 1.9: A schematic view of a flying wing with vertical and horizontal flight modes [1]

1.3.3 LTA vehicles

Balloons, airships, parafoil and parachute are all different types of LTA vehicles. Balloons and airships are flying configurations which had important role during space exploration in the past decades. A flying balloon needs simple technology to be designed and manufactured. In addition to that, it does not need power to maintain the altitude. These flying objects apply power only for instruments and payloads. They can change their altitude but they are not able to change their location. Balloons cannot stay in the Sun or keep their station and they do not have enough flexibility for atmospheric science. Airships compared to balloons have difficulty to stow and deploy. They are able to change their altitudes with slow speed. Same as balloons, airships cannot stay in Sun and keep their station, and they have too much complexity and too low flexibility[1].

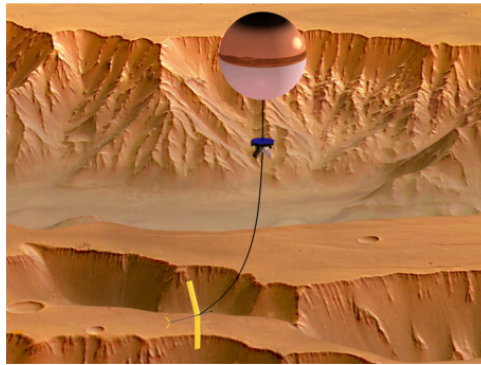


Figure 1.10: View of designed and manufactured Balloon Guidance System [1] for Mars exploration

The parafoil system, also called ram-air parachute, like others LTA vehicles is flexible and easy to design and manufacture, but is more controllable and have high glide ratios, which make it perfect to perform an autonomous precise landing on the surface of Mars. Parafoils have a ram-air inflated, double membrane airfoil cross section and are equipped for steering by means of wing tip or trailing edge lines [6]. Pulling the lines creates a difference of angle of attack at the wing tips, therefore different drag forces which generate a yaw moment. This technology is widely used on Earth already, some studies proposed to use this technology to land on Titan, as reported on [6], and the aim of this thesis is to demonstrate that could also be used for an autonomous rover landing on Mars.



Figure 1.11: Parafoil model. Credits: free3D.com

1.3.4 Flapping-wings

In recent years flapping winged aerobots for autonomous flight on Mars have been proposed. This innovative solution is based on the capability to generate high lift under low Reynolds number flight flapping the wings. This is possible due to the fact that a wingspan of 1 m on Mars operates with a similar Reynolds number of an insects on Earth. However these drones have an endurance problem [1], they require lot of power to fly, so they can be applied only in short range missions. Furthermore so far only allometric formulae extracted from natural birds and insects [1] were used to design flapping wings. Therefore, these empirical formulas should be revisited and modified, to optimize this configuration for the martian environment.

An example of flapping wing drone is the *Entomompter* designed by Colozza and shown in Figure 1.12.



Figure 1.12: View of Entomompter designed by Colozza [1] for Mars exploration

Lift and thrust, in fact, are directly related to density by the following formulas:

$$L = \frac{1}{2}\rho V^2 C_L S \quad (2.1)$$

$$T = \frac{1}{2}\rho V_{tip}^2 C_T A \quad (2.2)$$

Where L is the lift force, ρ is the atmospheric density, V is the air speed, C_L is the coefficient of lift for the vehicle, S is the reference surface area, T is rotor thrust, C_T is the coefficient of thrust, A is the area of the rotor, and V_{tip} is the speed of the rotor tip [10]. As the density is a hundred times lower than on Earth, generating thrust is much more difficult. This implies that aerobots generally have larger dimensions and heavier weights than those on the ground. For greater understanding, the main parameters influencing flight are listed below:

Table 2.1: Comparison of Relevant Earth and Mars Parameters [10]

	Earth	Mars
Gravity (m/s²)	9.81	3.71
Atmospheric Composition	N ₂ 78.08%	N ₂ 2.7%
	O ₂ 20.95%	O ₂ 0.13%
	H ₂ O 0-4 %	CO 0.08 %
	Ar 0.93%	Ar 1.6%
	CO ₂ 0.036%	CO ₂ 95.32%
Atmospheric Density (kg/m³)	1.225	0.0138
Average Temperature (K)	288.15	210.15
Average Wind Speed (m/s)	0 - 100	2 - 30 (dust storm)
Speed of Sound (m/s)	340.3	245
Dynamic Viscosity	1.789 x 10 ⁻⁵	1.2235 x 10 ⁻⁴

As can be seen from the low average temperature and atmospheric composition, the speed of sound on Mars is lower than on Earth. This leads to a higher rotor tip Mach number, in the case of rotors. Indeed:

$$M_{tip} = \frac{V_{tip}}{\sqrt{\gamma RT}} \quad (2.3)$$

Where M_{tip} is the rotor tip Mach number, γ is the ratio of specific heats of the gas, R is the molar gas constant, and T is the temperature of the air. It's easy to understand how this limits the propellers angular speed and therefore also the maximum thrust that can be generated, in fact, Mach can't exceed a certain value or the flow would be detached causing lift losses.

This results in constraints that must be satisfied and which heavily influence the physical model of the aerobots. The figure 2.2 shows the variation of thrust as the M_{tip} varies on Earth and Mars.

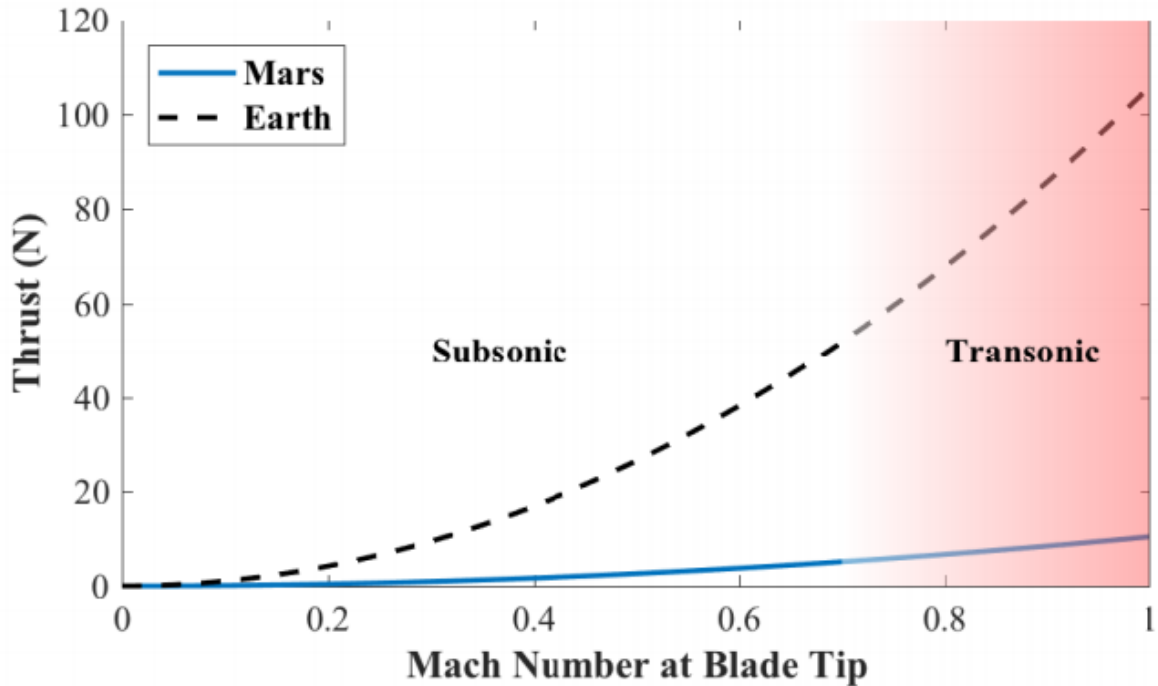


Figure 2.2: A Comparison of Rotor Thrust Generated on Earth and Mars [10]

Like the rotors, flying vehicles also have problems linked to the environment; the same amount of CO_2 is not present on Earth as on Mars. Because of this, the 'Red Planet' has a higher dynamic viscosity, which implies lower Reynolds numbers described by the equation 2.4.

$$Re = \frac{\rho V L}{\mu} = \frac{V L}{\nu} \quad (2.4)$$

Where Re is the Reynolds number, μ is the dynamic viscosity, ν is the kinematic viscosity, and L is the reference length. For comparison, aircraft flying in this Reynolds number regime on Earth include small Unmanned Aerial Vehicles (UAV) and Micro Air Vehicles (MAV) [12].

In view of this, it is necessary to study these effects well and recreate models of them as faithfully as possible.

2.2 Reference frame

In this section the reference systems that are used below and the mathematical operations to bind the state variables in the different reference frames are discussed for greater clarity.

2.2.1 Mars Inertial Frame

The Martian Inertial frame (MI) is a North-East-Down frame with the x and y axes lying on the local martian horizontal plane with the origin at the aerobot's CoM. The x axis is aligned with local martian North and the y axis is aligned with local martian East, while the z axis is oriented to form a right-handed triad. Values described in the MI frame are denoted $[\]_I$ [10].

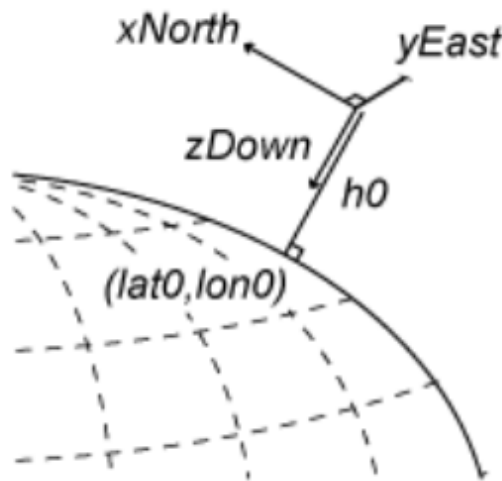


Figure 2.3: Mars Inertial Reference System

2.2.2 Body Frame

The body frame is fixed to the aerobot with its origin at the aerobot's CoM. The x axis is aligned with the aerobot's nose. The z axis points down through the center of the drone opposite to the rotor plane in the case of the drone, while it is directed along the joint of the centres of mass between the wing and the payload, towards the latter, in the case of the parafoil. Finally, the y -axis is directed to form a right-handed orthogonal triad. Values described in the body frame are denoted $[\]_B$ [10].

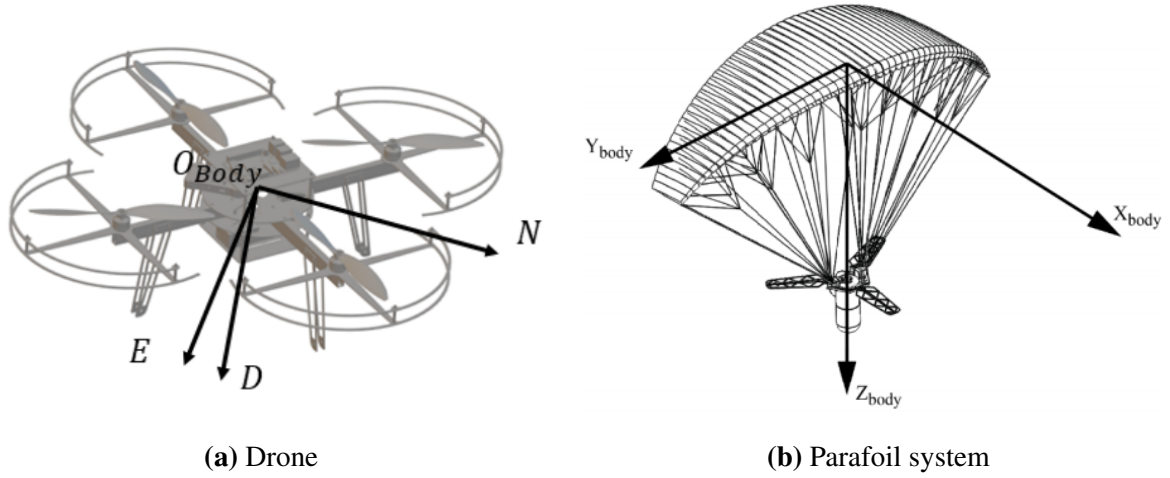


Figure 2.4: Body Reference Frame for drone and parafoil system

It's possible to switch from one reference system to another using the appropriate rotation matrices:

$$\mathbf{R}_I^B = \mathbf{R}_1(\phi)\mathbf{R}_2(\theta)\mathbf{R}_3(\psi) \quad (2.5)$$

$$\mathbf{R}_B^I = (\mathbf{R}_I^B)^T = \mathbf{R}_3^T(\psi)\mathbf{R}_2^T(\theta)\mathbf{R}_1^T(\phi) \quad (2.6)$$

\mathbf{R}_I^B is used to switch from the MI system to the body's one, where ϕ is the roll angle, θ is the pitch angle and ψ is the yaw angle. All together they are called *Euler's angles*. Each angle indicates the rotation to perform to align the two reference frames. The rotational matrices are defined as:

$$\mathbf{R}_1(\phi) = \begin{bmatrix} 1 & 0 & 0 \\ 0 & \cos(\phi) & \sin(\phi) \\ 0 & -\sin(\phi) & \cos(\phi) \end{bmatrix} \quad (2.7)$$

$$\mathbf{R}_2(\theta) = \begin{bmatrix} \cos(\theta) & 0 & -\sin(\theta) \\ 0 & 1 & 0 \\ \sin(\theta) & 0 & \cos(\theta) \end{bmatrix} \quad (2.8)$$

$$\mathbf{R}_3(\psi) = \begin{bmatrix} \cos(\psi) & \sin(\psi) & 0 \\ -\sin(\psi) & \cos(\psi) & 0 \\ 0 & 0 & 1 \end{bmatrix} \quad (2.9)$$

2.3 Gravity model

Gravity on Mars is about one third of that on Earth, as mentioned above. Due to Mars' ellipsoid shape the gravitational acceleration is not uniformly distributed over the planet, being particularly intense at the poles. There are kilometer level resolution models that allow to observe how gravity varies on the planet's surface [13].

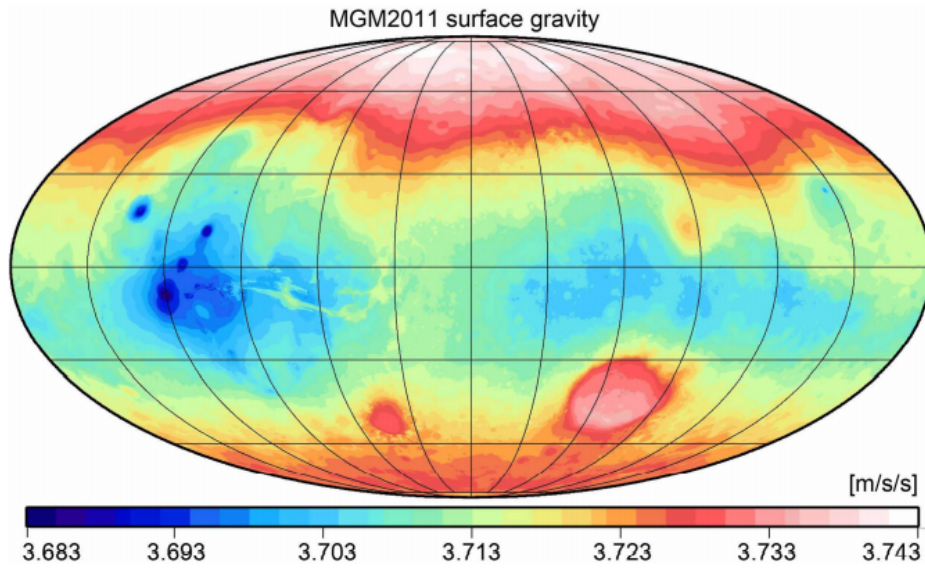


Figure 2.5: Global Gravity Map of Mars [13]

As can be seen from the graph, the variation of gravitational acceleration is not such as to significantly affect the dynamics of an aerobot, so we can assume the gravity acceleration as a constant $g = 3.72 \text{ [m/s}^2\text{]}$. In particular, in the developed model, the force generated by gravity is expressed in a NED system:

$$\vec{F}_g = \begin{bmatrix} 0 \\ 0 \\ mg \end{bmatrix}_I \quad (2.10)$$

However, for the calculations carried out, it is necessary to relate the force in body axes through the appropriate rotation matrices, obtaining:

$$\mathbf{R}_I^B \vec{F}_g = \begin{bmatrix} -mg \sin(\theta) \\ mg \cos(\theta) \sin(\phi) \\ mg \cos(\theta) \cos(\phi) \end{bmatrix} \quad (2.11)$$

2.4 Atmosphere model

The martian atmosphere consists of a thin layer of gas, it is not uniform and the properties of the fluids change as a function of time and the geographical area selected. However, the main variations depend on the altitude in relation to the martian soil itself. In particular, the Sun heats the surface and part of this heat is transmitted to the gas near the surface which is then diffused or convected up through the atmosphere. Thus, the gas temperature is highest near the surface and decreases as we increase altitude. Furthermore, as with the Earth, the pressure of the atmosphere decreases with increasing altitude while the density depends on the first two factors mentioned.

In order to perform simulations and understand the variation of these parameters, the Mars Global Surveyor developed a model in April 1996. Information on the martian atmosphere was collected by Jonathon Donadee of Canfield (Ohio) Middle School during a cyber-mentoring programme in 1999. The model has two zones with separate curves suitable for the lower and upper atmosphere. The lower atmosphere runs from the surface of Mars to 7,000 meters [14].

$$T [C^\circ] = \begin{cases} -31 - 0.000998h, & \text{if } h \leq 7000m \\ -23.4 - 0.00222h, & \text{if } h > 7000m \end{cases} \quad (2.12)$$

$$p = 0.699e^{-0.00009h} [kPa] \quad (2.13)$$

$$\rho = k \left(\frac{p}{0.1921(T + 273.1)} \right) \left[\frac{kg}{m^3} \right] \quad (2.14)$$

Where the parameter k depends on the chosen geographical area, the time and the period of the year. While the value 0.1921 is the specific gas constant \bar{R} is expressed as Kjoule/(Kg kelvin). The model, clearly, could be replaced by a more accurate one in the future, but for a preliminary analysis it is quite accurate.

2.5 Wind model

The atmospheric changes described above cause wind on Mars.

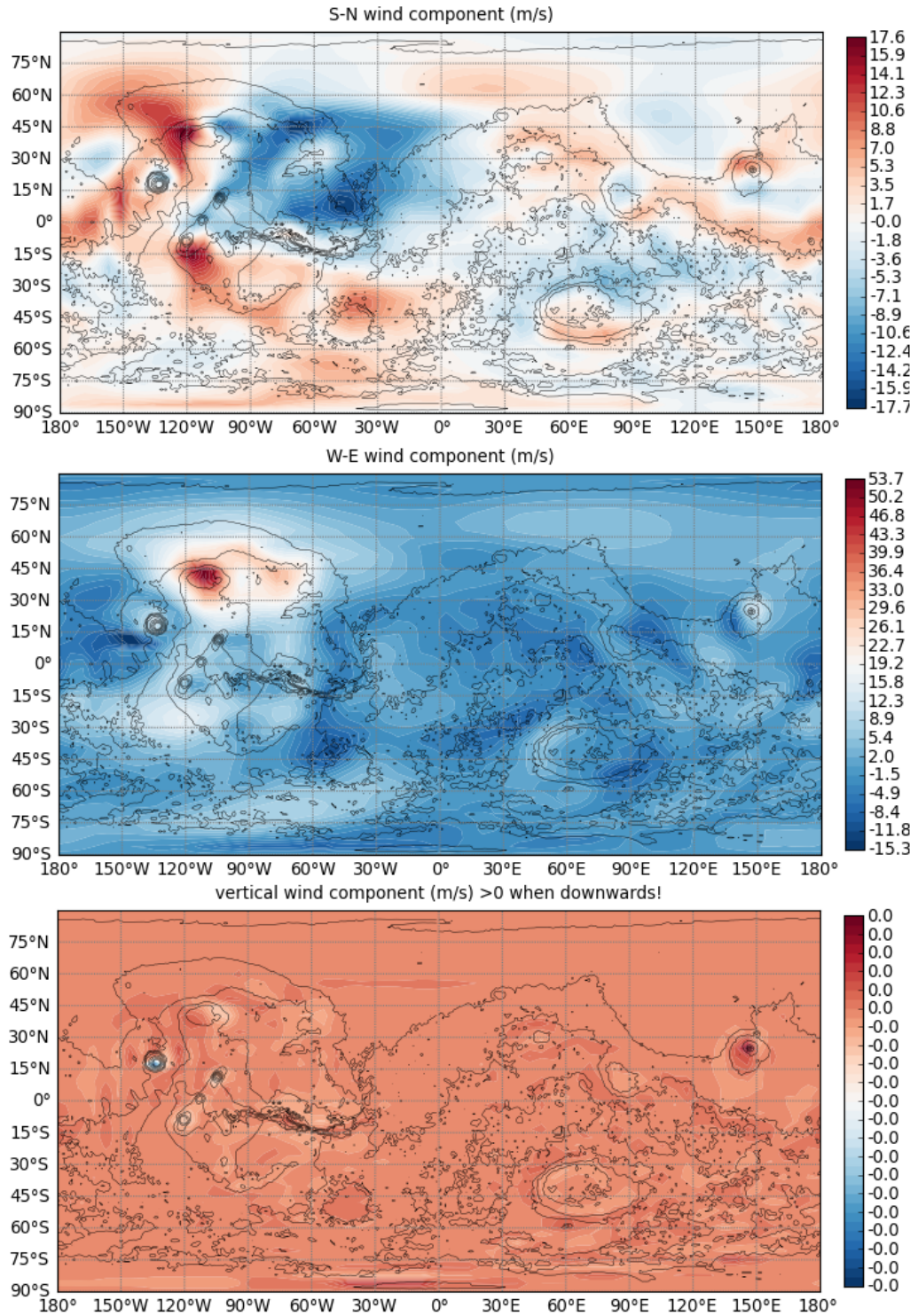


Figure 2.6: Average wind in Mars during winter at 10m altitude [5]

It varies with the seasons, the time of day and even altitude. In order to understand its trend, reference is made to the Mars Climate Database [5]. To create a functional model, it has been chosen to observe the wind trend in the 3 directions of the MI frame for different seasonal periods, assuming as landing point the *Gale Crater*, which is the same as *Curiosity*, then the 3 average components that best represent the wind trend have been chosen:

- **Wind in vertical direction** set equal to $2.3 \cdot 10^{-4}$ m/s,
- **Wind in South/North direction** set equal to 6.08 m/s,
- **Wind in West/East direction** set equal to 0.87 m/s.

However, having a constant wind in modulus and direction is not a truthful representation of real condition. In such a case one could not evaluate the ability of the controller to react to a continuously varying and random perturbation. So a model is created where two disturbance components are added to a random constant component to recreate the wind behavior, in the following cases the value used is not one of the three previously chosen because the model works exactly in the same way a priori of the average value to which it is chosen to add the disturbances:

- The **Bias** is generated through an uniformly distributed random signal equal to $\pm 10\%$ of average wind value, its value changes at each integration step, so its frequency is equal to that of the dynamics of the system,

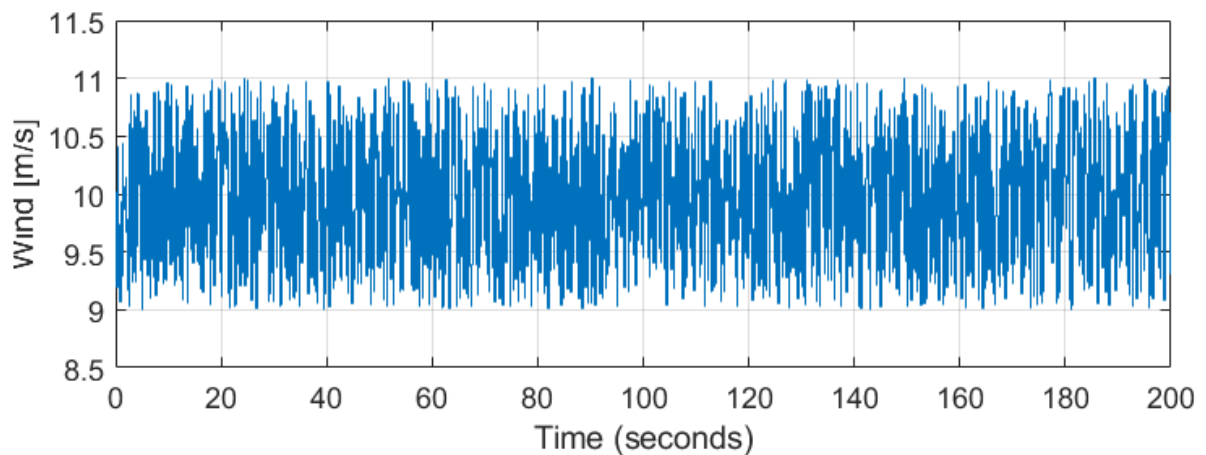


Figure 2.7: Average wind with Bias of 10%

- The **White Noise** is added to the wind with bias as an additional disturbance generated by a gaussian distribution, like the previous one it works at the same frequency of the dynamic equations.

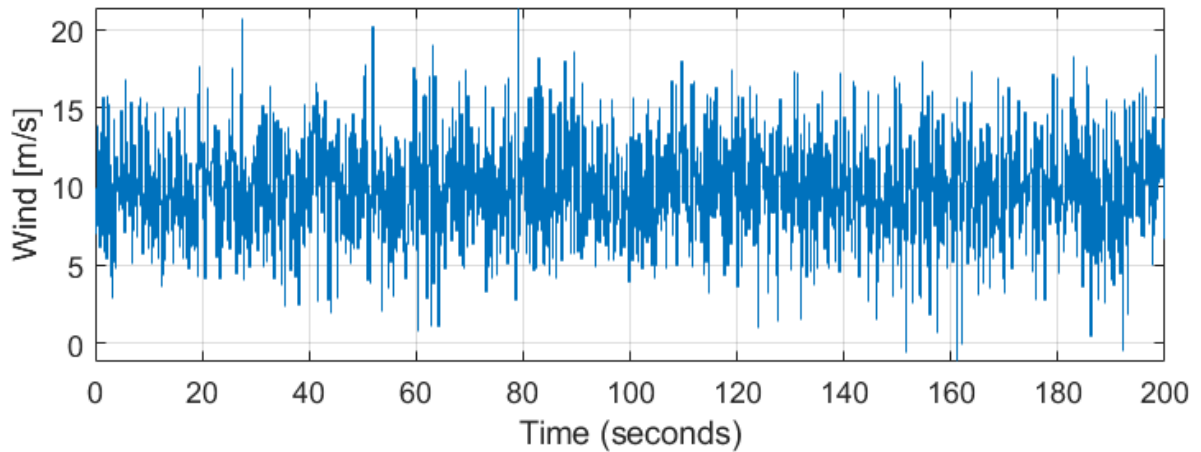


Figure 2.8: Average wind with Bias of 10% and Noise

Then the model adopted inside the simulator introduces the components in vectorial form. The conceptual diagram of how the wind model works is shown in the figure 2.9:

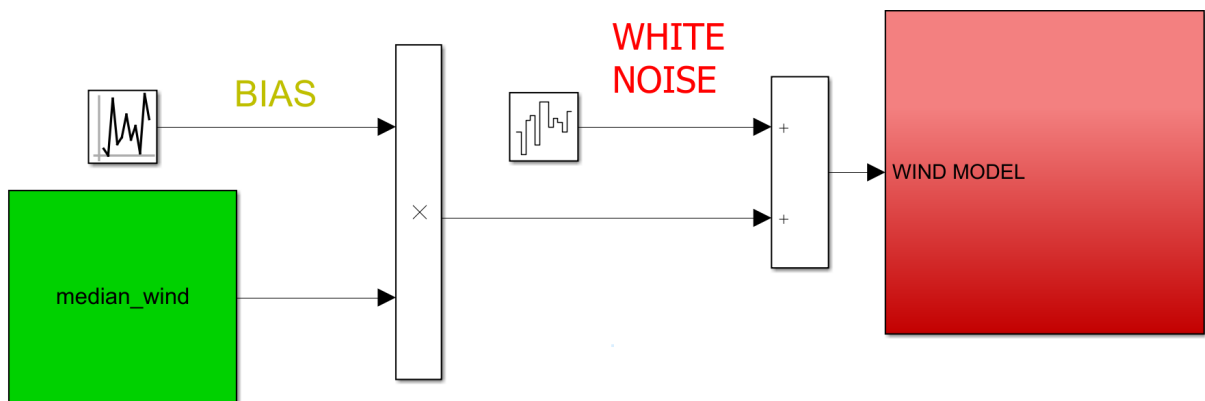


Figure 2.9: Wind model operating diagram

Where *Median wind* is a vector containing the 3 selected mean wind values.

2.6 Drone's models

There are various configurations in which a multicopter can appear, each of which has its merits and demerits, as well as various mathematical models representing the evolution of its motion:

- **Bicopter**'s composed by two rotors and for this reason is the least stable and is difficult to tune. It is also the one that produces the least lift in its category, in fact it has the fewest propellers [15],



Figure 2.10: Example of Bicopter

- **Tricopter** are considered the least expensive type of multicopter both because they have only three motors and because they require servo motors which are much less expensive than brushless motors. Another advantage is the wider angle (120 degrees) between the two front motors, which makes it easy to do in-air videography while the propellers remain out of sight. Typical rotor's configurations are "T" or "Y" shaped. Two propellers which are on the front arms pointed to the sides or slightly forwards, and one arm backwards. The latter can be rotated by means of a suitable bracket to control yaw. However, the major problem with this type is that, as with the bicopters, it is not capable of withstanding failure [15],



Figure 2.11: Example of Tricopter "Y" shaped

- **Quadcopter** consists of 4 rotors mounted on arms located in the same plane at 90 degrees to each other. There are two sets of Clockwise (CW) and Counter Clockwise (CCW) propellers mounted on the motors to create opposite force to balance it. The main advantages of quadcopters over other copters are that they do not require mechanical linkages to vary the rotor blade pitch angle as they stroll or spin. This makes design of quadcopter simple and stable. For the same lift generated, the quadcopter has four rotors, each of which is smaller than that of a helicopter. This reduces the probability of damage as the centripetal force on each rotor is lower [15]. For this work, two different configuration are analyzed:
 - *Quad + configuration* is the easiest to control; the rotor arms are arranged along the x,y body axes but in this case none of the directions of movement correspond to the focal axis of a possible optical system, since if this were the case the view would be obstructed by the rotors themselves,
 - *Quad × configuration* is the most appropriate to support a payload to scan the environment; the rotor arms are arranged to form the bisectors of the x,y body axes.

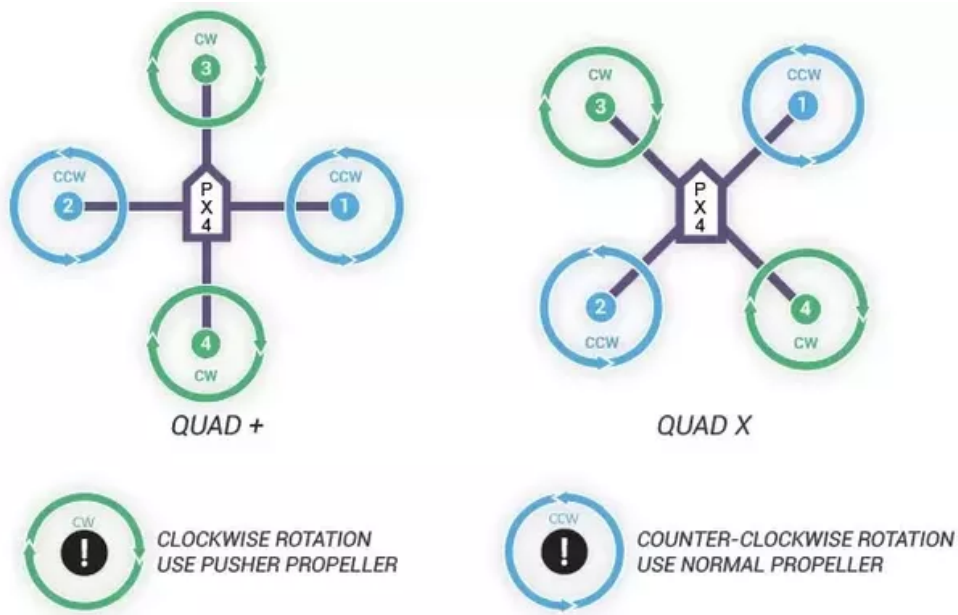


Figure 2.12: Example of Quadcopter "+" and "x" shaped [15]

In this work the quadcopter \times configuration and the equations governing its motion are discussed. In particular, the evolution of the motion of this body is governed by kinematic and dynamic models.

2.6.1 Kinematics model

The kinematics model represent all those equations needed to move from one reference system to another. The main variables are:

- Euler angles and angular velocities in the inertial frame,

$$\dot{E} = [\dot{\phi}, \dot{\theta}, \dot{\psi}]^T \quad (2.15)$$

- Angular velocity in body reference frame.

$$\omega = [p, q, r]^T \quad (2.16)$$

In the subsection 2.2.2 is shown how to change the reference system; however the matrices presented permit changing the position coordinates but not the angular or translational velocities in the two references. For this reason it's necessary to find a relationship between the Euler angles characterizing the quadrotor attitude w.r.t. the inertial frame and the angular velocities p , q and r in the body reference frame. It is obtained that:

$$\begin{bmatrix} \dot{\phi} \\ \dot{\theta} \\ \dot{\psi} \end{bmatrix} = \begin{bmatrix} 1 & s_{\phi}t_{\theta} & c_{\phi}t_{\theta} \\ 0 & c_{\phi} & -s_{\phi} \\ 0 & \frac{s_{\phi}}{c_{\theta}} & \frac{c_{\phi}}{c_{\theta}} \end{bmatrix} \begin{bmatrix} p \\ q \\ r \end{bmatrix} \quad (2.17)$$

Where:

$$\cos(\cdot) = c_{(\cdot)} \quad \sin(\cdot) = s_{(\cdot)} \quad \tan(\cdot) = t_{(\cdot)} \quad (2.18)$$

Furthermore, Euler angles are not the only set of coordinates for defining the drone orientation. In fact, when $\theta = \pi/2$ or so, it is possible to encounter a numerical instability, the denominator of some elements of the above matrix goes to zero: this problem called *Gimbal Lock*. From a physical point of view it consists in the loss of one degree of freedom in a three-dimensional caused when the axes of two of the three gimbals are driven into a parallel configuration and it becomes impossible to distinguish them.

This is why quaternions are used. They haven't singularity and are defined as follows:

$$\mathbf{q} = q_0 + q_1\mathbf{i} + q_2\mathbf{j} + q_3\mathbf{k} \quad \text{with} \quad \mathbf{ijk} = 1 \quad (2.19)$$

Where q_0 is a scalar value and q_1, q_2, q_3 are the component of the vector \mathbf{q} However, quaternions have not been used in this discussion because the drone modeled here is unlikely to achieve such high attitude angles.

2.6.2 Dynamics model

The dynamics model describe the rotational and translational dynamics of the aerobot taking into account forces and moments generated by the motion of the rotors, aerodynamic forces and moments acting on the body, and any cross-coupling effects produced from the relative motion of the four rotors and body. To develop a simple model, however, simplifying assumptions must be made, in order to have second order ordinary differential equation (ODE) [16]:

1. The quadrotor and all its components (i.e. propellers, motors...) are considered as rigid bodies,
2. The quadrotor CoM is the origin of the body reference frame,
3. The actuators are not modeled,
4. The aerodynamic forces are not considered,
5. The planet is considered as flat and its rotation is negligible w.r.t. body angular speeds.

Therefore, it is necessary to describe the translational and rotational dynamics:

- **Traslational dynamics** is based on Newton's Second Law

$$\mathbf{F} + \mathbf{R}_I^B m\mathbf{g} = m \left[\frac{d\mathbf{v}_B}{dt} + \boldsymbol{\omega}_B \times \mathbf{v}_B \right] \quad (2.20)$$

Where:

- v_B is the relative velocity of the quadrotor CoM w.r.t. air mass, defined as $\mathbf{v}_B =$

$$\begin{bmatrix} u \\ v \\ w \end{bmatrix}$$

- \mathbf{F} is a vector containing the propulsive thrust given by rotors

- $\boldsymbol{\omega}_B \times$ is defined as $\boldsymbol{\omega}_B \times = \begin{bmatrix} 0 & -r & q \\ r & 0 & -p \\ -q & p & 0 \end{bmatrix}$

Explicitly expressing the acceleration from this formula, it is possible, by integrating it, to derive the speed of the drone

$$\dot{\vec{V}}_B = \frac{1}{m} \left(\begin{bmatrix} -mgs\theta \\ mgc\theta s\phi \\ mgc\theta c\phi \end{bmatrix} + \begin{bmatrix} F_X \\ F_Y \\ F_Z \end{bmatrix} \right) - \vec{\omega}_B \times \vec{V}_B \quad (2.21)$$

- **Rotational dynamics** is based on Euler's Rigid Body Equations

$$\boldsymbol{\tau} = \left(\frac{d\mathbf{H}}{dt} + \boldsymbol{\omega}_B \times \mathbf{H} \right) \quad (2.22)$$

Where

- $\boldsymbol{\tau}$ is a vector of the moment acting on the drone
- \mathbf{H} is the vector containing the component of the angular momentum defined as

$$\mathbf{H} = \mathbf{J}\boldsymbol{\omega}_B = \begin{bmatrix} J_x & J_{xy} & J_{xz} \\ -J_{xy} & J_y & -J_{yz} \\ -J_{xz} & -J_{yz} & -J_z \end{bmatrix} \begin{bmatrix} p \\ q \\ r \end{bmatrix}$$

By making the angular acceleration explicit, it is possible to calculate the angular velocities of the drone in body axes by integrating them.

$$\dot{\boldsymbol{\omega}}_B = -\mathbf{J}^{-1} (\boldsymbol{\omega}_B \times (\mathbf{J}\boldsymbol{\omega}_B)) + \mathbf{J}^{-1}\boldsymbol{\tau} \quad (2.23)$$

2.7 Parafoil's models

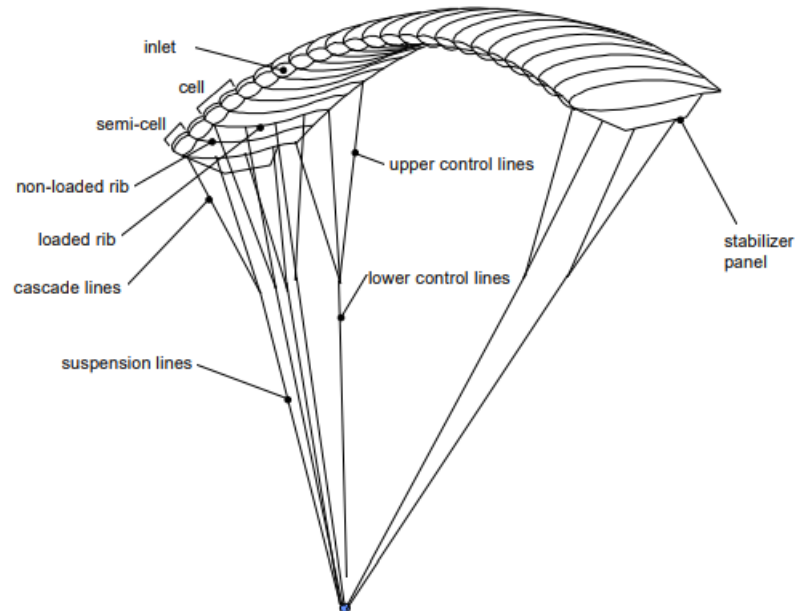


Figure 2.13: The ram-air parachute [17]

Several approaches can be used to describe the dynamics of a parafoil with a suspended payload. 3 to 6 DoF models use simplified aerodynamics (steady coefficients), constant drag area for payload, simplified added mass effects and two-dimensional wind models [18]. 9 to 15 DoF models are more accurate, but require more accurate estimations of aerodynamic coefficients, lines elasticity and, eventually, joint or hinge modelling, if present [18]. In this section a 6 DoF model used to represent the parafoil system is discussed. It's a good compromise between computational complexity and accurate solutions. In this model parafoil and payload (vehicle) are considered to be a single rigid body. This assumption is reasonable if the parafoil is completely inflated and the suspension lines are completely stretched [18].

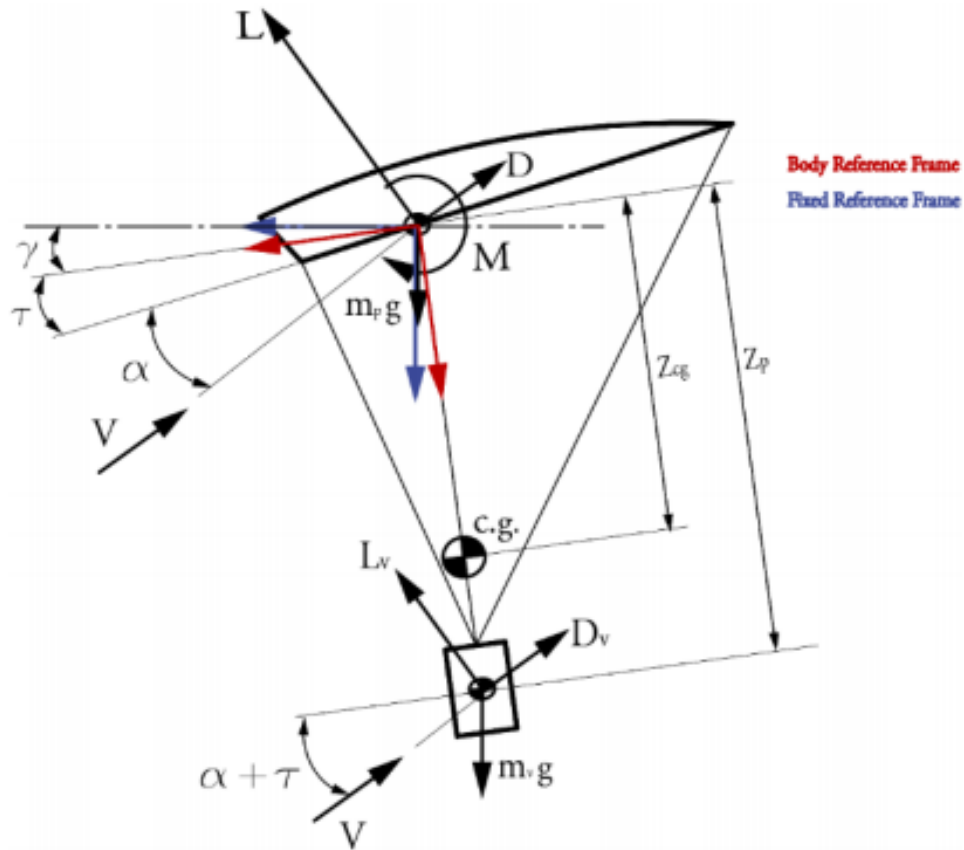


Figure 2.14: Free body configuration of the parafoil-payload system [18].

2.7.1 Kinematics model

The kinematics variables are three Euler orientation angles and three directional velocities, that can be represented in inertial and body frame:

$$V = [u, v, w]^T \quad \omega = [p, q, r]^T \quad (2.24)$$

$$\dot{N}_{av} = [\dot{x}_N, \dot{x}_E, \dot{h}]^T \quad \dot{\Phi} = [\dot{\phi}, \dot{\theta}, \dot{\psi}]^T \quad (2.25)$$

V and ω represent the velocity and angular velocity in the body frame, which is centered in the CoM of the parafoil, as presented in figure 2.4b. While \dot{N}_{av} and $\dot{\Phi}$ are the velocity and angular velocity in the NED inertial frame. The variables in the two frames are linked to each other through the rotational matrix R_B^I (eq. 2.6) and its derivative:

- **Navigation equations**

$$\dot{N}_{av} = \begin{Bmatrix} \dot{x}'_N \\ \dot{x}'_E \\ \dot{h} \end{Bmatrix} = [R_B^I] \begin{Bmatrix} u \\ v \\ w \end{Bmatrix} \quad (2.26)$$

- **Angular Kinematics equations**

$$\dot{\Phi} = \begin{Bmatrix} \dot{\phi} \\ \dot{\theta} \\ \dot{\psi} \end{Bmatrix} = [R_B^I]' \begin{Bmatrix} p \\ q \\ r \end{Bmatrix} \quad (2.27)$$

$$[R_I^B]' = \begin{bmatrix} 1 & 0 & -s_\theta \\ 0 & c_\phi & s_\phi c_\theta \\ 0 & -s_\phi & c_\phi c_\theta \end{bmatrix} \quad [R_B^I]' = \begin{bmatrix} 1 & t_\theta s_\phi & t_\theta c_\phi \\ 0 & c_\phi & -s_\phi \\ 0 & \frac{s_\phi}{c_\theta} & \frac{c_\phi}{c_\theta} \end{bmatrix} \quad (2.28)$$

Where:

$$\cos(\cdot) = c_{(\cdot)} \quad \sin(\cdot) = s_{(\cdot)} \quad \tan(\cdot) = t_{(\cdot)} \quad (2.29)$$

2.7.2 Dynamics model

In general, since the payload and parafoil are considered a single rigid body, the following equations can be applied:

$$\sum \begin{Bmatrix} F_x \\ F_y \\ F_z \end{Bmatrix}_{ext} = m \left(\begin{Bmatrix} \dot{u} \\ \dot{v} \\ \dot{w} \end{Bmatrix} + [\omega] \begin{Bmatrix} u \\ v \\ w \end{Bmatrix} \right) \quad (2.30)$$

$$\sum \begin{Bmatrix} M_x \\ M_y \\ M_z \end{Bmatrix}_{ext} = [J] \begin{Bmatrix} \dot{p} \\ \dot{q} \\ \dot{r} \end{Bmatrix} + [\omega][J] \begin{Bmatrix} p \\ q \\ r \end{Bmatrix} \quad (2.31)$$

Where $\{F_*\}_{ext}$ and $\{M_*\}_{ext}$ are the external forces and moments on the body, m is the total mass of the system, thus payload mass plus parafoil mass, and $[J]$ is the inertial tensor defined as:

$$[J] = \begin{bmatrix} (j_{xx_p} + j_{xx_v}) + mZ_{cg}^2 & - (j_{xy_p} + j_{xy_v}) & - (j_{xz_p} + j_{xz_v}) \\ - (j_{xy_p} + j_{xy_v}) & (j_{yy_p} + j_{yy_v}) + mZ_{cg}^2 & - (j_{yz_p} + j_{yz_v}) \\ - (j_{xz_p} + j_{xz_v}) & - (j_{yz_p} + j_{yz_v}) & (j_{zz_p} + j_{zz_v}) \end{bmatrix} \quad (2.32)$$

Z_{cg} is represented in figure 2.14, the parameters j with index p are the moments of inertia of the parafoil, while the ones with index v are the moments of inertia of the payload.

The external forces and moments have three main contributions expressed in body frame: weight force and the weight induced moments (F_g, M_g), aerodynamic forces and moments (F_{aero}, M_{aero}) and the apparent mass contributions (F_{app}, M_{app}).

$$\sum \left\{ \begin{array}{c} F_x \\ F_y \\ F_z \end{array} \right\}_{ext} = F_{aero} + F_{app} + F_g \quad (2.33)$$

$$\sum \left\{ \begin{array}{c} M_x \\ M_y \\ M_z \end{array} \right\}_{ext} = M_{aero} + M_{app} + M_g$$

Weight force and moments

The weight force and the weight induced moments are so expressed:

$$F_g = m \cdot [R_I^B] \left\{ \begin{array}{c} 0 \\ 0 \\ g \end{array} \right\} \quad (2.34)$$

$$M_g = \begin{bmatrix} -mgZ_{cg} \sin \phi \cos \theta \\ -mgZ_{cg} \sin \theta \\ 0 \end{bmatrix}$$

Aerodynamic forces and moments

Both the parafoil and the payload give an aerodynamic contribution. Obviously the payload's contribution is lower, but not negligible. The aerodynamic forces and moments are described using a formulation based on aerodynamic derivatives [18], which can be non-linear, but with a 6 DoF model they can be considered steady.

$$F_{\text{aero}} = F_{\text{aero parafoil}} + F_{\text{aero vehicle}}$$

$$F_{\text{aero parafoil}} = L_p \begin{bmatrix} \sin(\alpha + \tau) \\ 0 \\ -\cos(\alpha + \tau) \end{bmatrix} - D_p \begin{bmatrix} \cos(\alpha + \tau) \\ 0 \\ -\sin(\alpha + \tau) \end{bmatrix} + \begin{bmatrix} 0 \\ Y_p \\ 0 \end{bmatrix}$$

$$L_p = \frac{1}{2}\rho V_T^2 SC_L \quad (2.35)$$

$$D_p = \frac{1}{2}\rho V_T^2 SC_D$$

$$Y_p = \frac{1}{2}\rho V_T^2 SC_Y$$

$$F_{\text{aero vehicle}} = \frac{1}{2}\rho V_T^2 \begin{bmatrix} SC_x \\ SC_y \\ SC_z \end{bmatrix}$$

$$M_{\text{aero}} = M_{\text{aero parafoil}} + M_{\text{aero vehicle}}$$

$$M_{\text{aero parafoil}} = \frac{1}{2}\rho V_T^2 S \begin{bmatrix} bC_l \\ cC_m \\ bC_n \end{bmatrix} \quad (2.36)$$

$$M_{\text{aero vehicle}} = \frac{1}{2}\rho V_T^2 S_v \begin{bmatrix} dC_l \\ dC_m \\ dC_n \end{bmatrix}$$

In these formulas V_T is the *free stream velocity*, which is seen by the parafoil with an inclination of α (angle of attack) plus τ (rigging angle of the parafoil). S_v and d are the payload reference area and reference length; S , b and c are the parafoil's wing area, wing span and wing chord.

All the moments and forces are dependent from aerodynamic coefficients, which depend from the geometry and aerodynamic features of the parafoil and they are composed of both stability and control derivatives. For a rectangular straight wing the coefficients can be written as:

- *Longitudinal dynamics parafoil's coefficients*

$$\begin{aligned}
 C_L &= C_{L,0} + C_{L,\alpha}\alpha \\
 C_D &= C_{D,0} + \frac{C_L^2}{\pi e AR} \\
 C_m &= C_{m,0} + C_{m,\alpha}\alpha + \frac{c \cdot q}{2V_T} C_{m,q}
 \end{aligned} \tag{2.37}$$

- *Lateral-directional parafoil's coefficients*

$$\begin{aligned}
 C_Y &= C_{Y,\beta}\beta + C_{Y,\delta_a}\delta_a \\
 C_l &= C_{l,\beta}\beta + C_{l,\delta_a}\delta_a + \frac{b \cdot p}{2V_T} C_{l,p} + \frac{b \cdot r}{2V_T} C_{l,r} \\
 C_n &= C_{n,\beta}\beta + C_{n,\delta_a}\delta_a + \frac{b \cdot p}{2V_T} C_{n,p} + \frac{b \cdot r}{2V_T} C_{n,r}
 \end{aligned} \tag{2.38}$$

The aerodynamic derivatives are difficult to estimate without wind tunnel tests or CFD simulations. Since this is a preliminary study it has been decided to use values of a similar existing parafoil. Furthermore a ram-air parachute is not a straight wing, but as an arc shape, thus this geometry as an effect on the aerodynamic, in particular on the *longitudinal dynamics coefficients*.

Apparent mass effect

A ram-air parachute's structure is very light, which means that it is heavily influenced by the air passing over and around it. The pendulum motion of a parafoil system is affected since the point of rotation moves away from the CG of the system and towards the parafoil [19]. Usually for conventional aircraft this effect is negligible, but since the volume of air captured inside the parafoil is high, the moment of inertia and the inertia of the system increase considerably. The apparent mass effect can be computed with the simplified formulations in Ref [20]:

$$\begin{aligned}
 [K_{\text{app}}] &= \begin{bmatrix} A & 0 & 0 \\ 0 & B & 0 \\ 0 & 0 & C \end{bmatrix} \\
 [I_{\text{app}}] &= \begin{bmatrix} I_A & 0 & 0 \\ 0 & I_B & 0 \\ 0 & 0 & I_C \end{bmatrix}
 \end{aligned} \tag{2.39}$$

$$F_{app} = -[K_{app}] \dot{V} - \omega \wedge ([K_{app}] V) \quad (2.40)$$

$$M_{app} = -[I_{app}] \dot{\omega} - \omega \wedge ([I_{app}] \omega) - V \wedge ([K_{app}] V)$$

A , B , C and I_A , I_B , I_C are the volumes associated with the apparent masses and inertias for translation or rotation along each axis [20] represented in figure 2.15 and calculated with the equations:

$$A = 0.666\rho \left(1 + \frac{8}{3}\bar{a}^2\right) t^2 b$$

$$B = 0.267\rho \left(1 + 2\frac{\bar{a}^2}{t^2} AR (1 - \bar{t}^2)\right) t^2 c \quad (2.41)$$

$$C = 0.785\rho \sqrt{1 + 2\bar{a}^2 (1 - \bar{t}^2)} \frac{AR}{1+AR} c^2 b$$

$$I_a = 0.055\rho \frac{AR}{1+AR} c^2 b^3$$

$$I_b = 0.0308\rho \frac{AR}{1+AR} \left[1 + \frac{\pi}{6}(1 + AR)AR\bar{a}^2\bar{t}^2\right] c^4 b \quad (2.42)$$

$$I_c = 0.0555\rho (1 + 8\bar{a}^2) t^2 b^3$$

$$AR = \frac{b}{c} \quad \bar{t} = \frac{t}{c} \quad \bar{a} = \frac{a}{b} \quad (2.43)$$

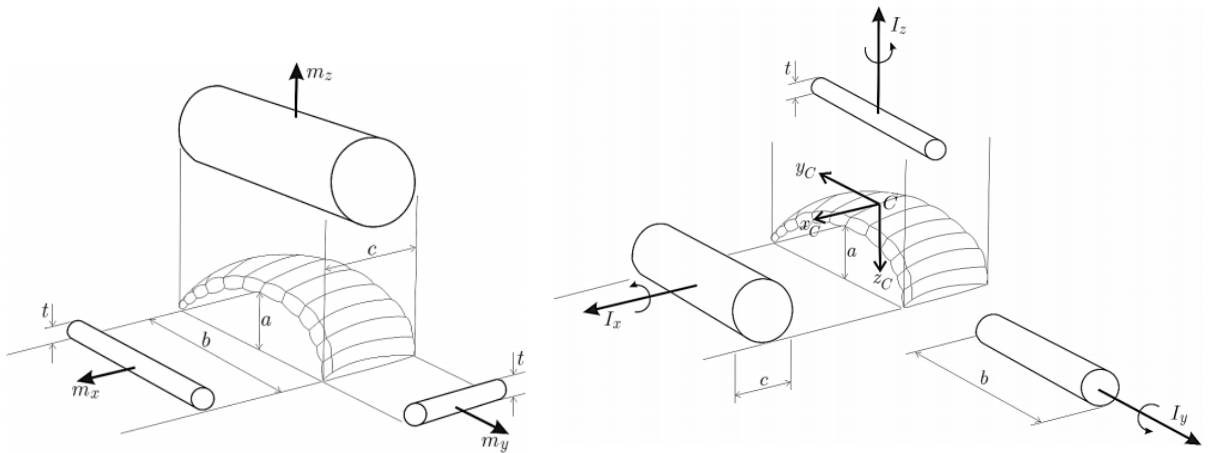


Figure 2.15: Volumetric Representation of Apparent Masses and Moments [20]

Obviously, as it can be seen in the equations 2.41 and 2.42, the apparent masses and inertias are dependent from the atmospheric density ρ . On Mars ρ is nearly 100 times lower than on Earth, for this reason the contribution of the apparent mass effect is negligible, as shown in the table below. Therefore the parafoil's dynamics simulator, developed in this thesis, doesn't take into account its contribution.

Table 2.2: Apparent masses and inertias comparison between Earth and Mars for a parafoil of 13 m² wing surface

	Earth	Mars
ρ kg/m ³	1.225	0.015
A kg	2.322	0.028
B kg	1.136	0.014
C kg	31.082	0.381
I_A kgm ²	53.333	0.654
I_B kgm ²	5.929	0.073
I_C kgm ²	18.915	0.232

3. Drone's dynamics simulator

The mathematical model is only one part of the simulator; it describes the evolution of the drone's motion. However, to complete the simulator it is necessary to physically characterize the drone and select an appropriate guidance and control algorithm. This chapter discusses the procedures carried out for the sizing of the drone and subsequently the implementation and tuning of the guidance and control algorithms. In fact, for the chosen mission, an autonomous system is considered. In figure 3.1 is shown the final structure of the simulator which is divided into 4 main blocks:

- *Motion's Equation* that contains the gravity , the atmosphere and the drone's model discussed respectively in the Sections 2.3, 2.4 and 2.6;
- *Actuators* which includes the model of the electric motors;
- *Sensors* that simulates wind disturbances discussed in Section 2.5.
- *Guidance & Control* that contains Guidance & Control algorithms that lead the drone towards the desired target by receiving as input the vector of states read by the sensors and returning to the actuators the actions that they must perform.

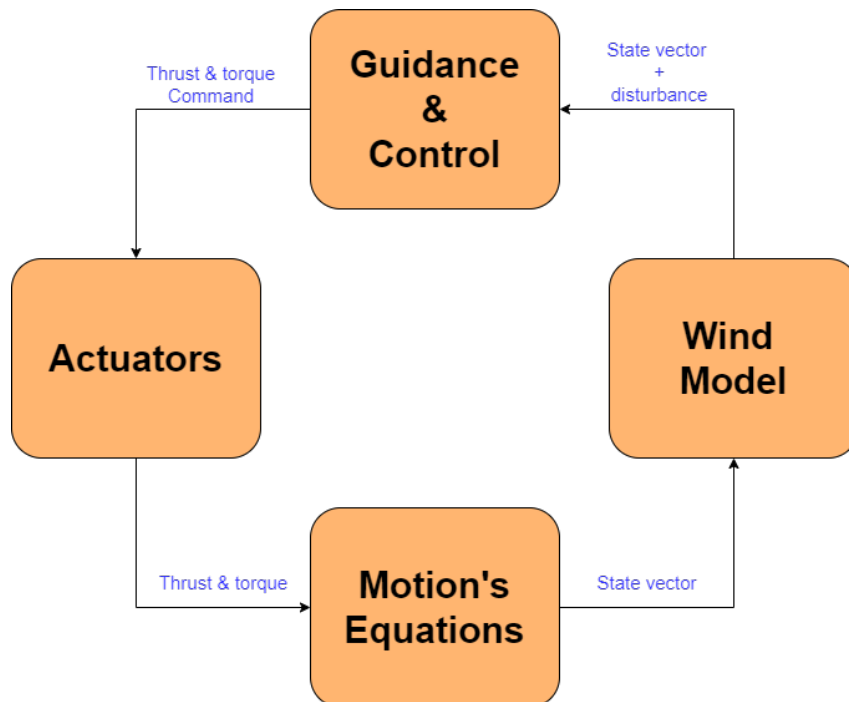


Figure 3.1: Drone's simulator

3.1 Drone configuration

Once the *Equations of Motion* has been implemented, some parameters should be defined. They depend on the physical structure, geometry, choice of motors and propellers and their relative coupling. Therefore choosing the number of propellers and their arrangement, as done before, is not sufficient to complete the mathematical model but are just some inputs. These parameters are closely linked, so if the input data are not sufficient to define them uniquely, iterative loops must be used.

3.1.1 Propellers

The aerodynamic characterisation of the propeller is an important step to determine the propulsive capabilities of the drone. This can be done using the *Blade Elementary Theory* (BET), which predicts the value of force, torque and mechanical power required by the propellers [21]. However, for COTS propellers, it is not always easy to find all the geometric data needed to perform BET. For this reason, experimental data obtained in the wind tunnel are fundamental as they provide a complete view of the propeller's performance [21], [22]. Tests were conducted under indoor conditions in the *TerraXcube*, a hypobaric climatic laboratory where is possible to set different extreme environmental conditions such as humidity, solar radiation, rain and snow temperature (from $-40C$ to $40C$) and pressure (from sea level up to $300mbar$ - $9000mbar$), in order to focus on how harsh environments (low temperature and pressure) influence unmanned vehicle performance. As result it's possible to relate the thrust and torque to the engine speed using the following equations:

$$c_T = \frac{T}{1/2\rho D^4 n^2} \quad (3.1)$$

$$c_Q = \frac{Q}{1/2\rho D^5 n^2} \quad (3.2)$$

Where

- T is the thrust
- Q is the propeller torque
- ρ is the air density
- n is the angular speed in rev/min
- D is the diameter of the propellers

c_T and c_Q are dimensionless quantities that are performance indicators of the drone. In this work, these values are equal to the reference [23].

It can be seen (figure 3.2) that the coefficients do not vary when the angular speed varies, but under the same conditions the system does not always have the same values; these depend strongly on the propeller/motor coupling. It has been assumed, therefore, to select a propeller and a motor that present the same characteristics.

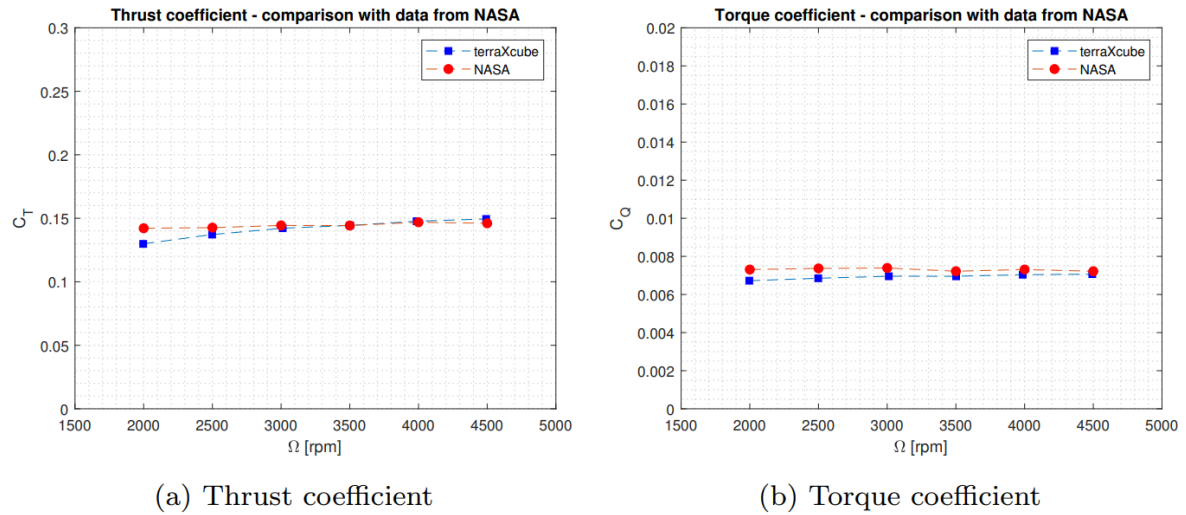


Figure 3.2: Values of C_t and C_q as the angular velocity varies [23]

Another fundamental step in propeller modelling is the determination of mass and geometry. To do this, data are collected for modeling helicopter propellers and drones. These are shown in the tables 3.2 and 3.1

Table 3.1: Helicopter's propellers data

Modeling Helicopter	radius(m)	cord(mm)	mass(kg)
ALIGN HD420F	0,425	0,042	0,12
ALIGN HD360A	0,36	0,033	0,054
ALIGN HD600E	0,6	0,055	0,27
ALIGN HD700BT	0,7	0,06	0,38
T-REX 450	0,325	0,032	0,044

Table 3.2: Drone's propellers data

DRONE PROP	D (m)	mass (kg)	max ω Earth (Mach 0.7)	R (m)	c (m)
48x16.4	1,2192	0,35	3800	0,6096	0,06096
40x13.3	1,016	0,18	4500	0,508	0,0508
32x10.6	0,8128	0,1	5600	0,4064	0,04064
30x10	0,762	0,071	6000	0,381	0,0381
28x9.4	0,7112	0,076	6400	0,3556	0,03556
26x8.7	0,6604	0,066	6900	0,3302	0,03302
24x8.1	0,6096	0,055	7500	0,3048	0,03048
22x7.4	0,5588	0,044	8200	0,2794	0,02794
20x6.7	0,508	0,03	9000	0,254	0,0254
18x6	0,4572	0,027	10000	0,2286	0,02286
17x5.7	0,4318	0,023	10600	0,2159	0,02159
15x5	0,381	0,018	12000	0,1905	0,01905
14x4.5	0,3556	0,019	12900	0,1778	0,01778

Max ω Earth indicates the rotation beyond which the blade tip reaches $Mach > 0.7$ with a density equal to that of the Earth at sea level. In fact, as the radius increases, the peripheral speed increases, making it easier to reach high Mach; having values too close to 1 would result in the detachment of the flow and loss of lift that would compromise the flight of the drone. This is a first limitation on the maximum size that propellers can have. However, taking into account equation 3.1 and remembering that Mars has a density one hundred times less than that of the Earth, such a large reduction in density leads to a large reduction in thrust unless the surface area capable of generating lift is increased. It is therefore necessary to find a good compromise between the two parts.

For the sake of completeness, in the graph is shown the trend in mass as a function of radius, comparing the data between the two tables. The interpolation provides two different curves, one linear, the other parabolic. Both are used to obtain the most accurate mass estimate possible.

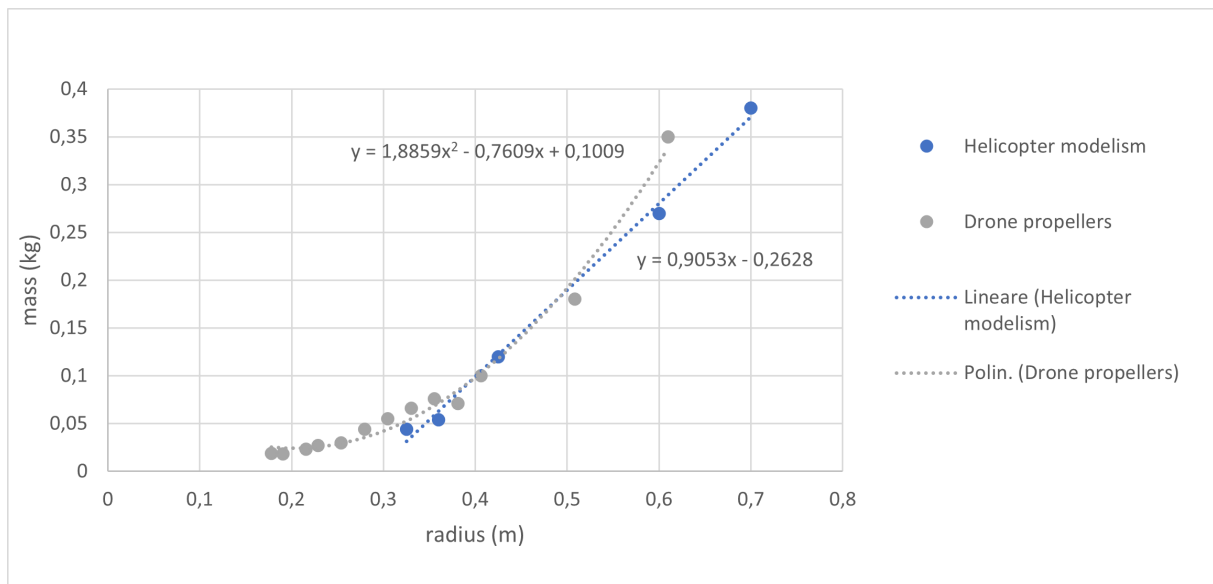


Figure 3.3: Mass as a function of radius for drone propellers and model helicopter propellers

The sizing of the physical and geometry characteristic of the drone led to the choice of a propeller with the following characteristics.

Table 3.3: Selected propeller's data

Radius	0,40 m
Mass	0.200 Kg
P max rot	6,01 W
Q max rot	0.0957 Nm
T max rot	2,24 N
omega max	3636 RPM
omega hover	2700 RPM
P max tot	24,04 W
P hover rot	2,15 W
P hover	8,6 W
P media	16,32 W

3.1.2 Electric motors and batteries

The sizing of the propeller involves the choice of a suitable electric motor capable of satisfying the torque and angular speed requirements. Brush-less type motors are selected, they are the ones that best suit the martian atmosphere and, in general, missions where it is not possible to do maintenance. Brush-less motors have 2 main configurations:

- Inner runners that rotate very fast, so they need a reducer to increase torque at the expense of angular speed,
- Outer runners produce more torque than their inner-runner counterparts. So they eliminate the extra weight, complexity, inefficiency and noise of a gearbox. This makes them the most suitable choice for a multi-rotor, but the real one limitation is the endurance in flight due to power source.

The choice of the type of motor depends strongly on the power required by the propeller. Each rotor needs a mechanical power in the case of maximum angular speed equal to:

$$P_m = Q \cdot \omega_{max} \quad (3.3)$$

Where Q is computed from equation 3.2 and ω_{max} is chosen from table 3.3 so that the Mach at the tip does not exceed 0.7.

The motor must be able to provide, therefore, an equal power, also considering losses and a non-unitary efficiency. In relation to this, along with an excellent power-to-weight ratio and the wide temperature range it can withstand, the DJI-E305 is selected as one of the possible motors [24].

Table 3.4: DJI E305 peculiarity

Temperature range	from -10 to 40 °C
Max voltage	17,4 V
Max current	20 A
Max peak current (3 seconds)	30 A
ESC mass	0,027 kg
Stator mass	0,056 kg

The maximum power the engine can withstand is:

$$P_w = V_{max} \cdot I_{max} \quad (3.4)$$

Where V_{max} is the maximum voltage and I_{max} is the maximum current.

In this way $P_w > P_m$.

The energy is obtained from the batteries through the conversion of electrochemical energy into electricity. There are two main types of batteries:

- *Primary batteries* have high performance but are not rechargeable,
- *Secondary batteries* have lower performance than primary's one but they are rechargeable. The most common type is lithium polymer.

When choosing a battery, several parameters should be taken into account:

- *Energy* is the total Watt-hours available when the battery is discharging given a certain discharge current (specified as a C-rate [r_C]). Energy is calculated by multiplying the discharge power (in Watts) by the discharge time (in hours). Like capacity, energy decreases with increasing C-rate,
- *Dept of Discharge (DoD)* is the percentage of battery capacity that has been discharged expressed as a percentage of maximum capacity,
- *Specific Energy* is the nominal battery energy per unit mass,
- *Capacity* is the amount of electric charge it can deliver at the rated voltage and is measured in units such as mamp-hour (mAh).

In fact, thanks to them it is possible to calculate the required current and from it, knowing the voltage, the power that the battery can supply.

$$P_b = V \cdot I \quad (3.5)$$

$$I = r_C \cdot C \quad (3.6)$$

Where r_c is the *Discharge rate* and C is the *capacity*. These parameters also allow to derive a possible flight time for each charge.

$$t_f = \frac{E}{P_m} \quad (3.7)$$

$$E = V \cdot C \quad (3.8)$$

Where E is the *Energy* expressed in Wh.

For completeness is reported the table with the values used for a lithium polymer battery.

Table 3.5: lithium polymer battery (Li-Po S4) peculiarity

Temperature range	from -20 to 60 °C
Capacity	1800 mAh
Discharge rate r_c	40 1/h
Voltage	14,8 A
Current	72 A
Energy density	1133,2 Wh/kg

Note how the current value is much higher than the maximum value tolerated by the single motor. It is worth remembering, however, that the same battery supplies power to the four motors of the drone, so each of them receives a quarter of current that is below the maximum tolerable limit. This happens because the battery cells are packed in series and therefore the motors at the input all see the same voltage, but a current, precisely, reduced.

3.1.3 Total mass and inertia tensor

The mass calculation involves the sum of 4 main elements:

1. **Battery mass** (m_b) can be calculated from the specific energy of the battery. Once the energy has been calculated, in fact, from the following formula it is possible to obtain its weight:

$$m_b = \frac{E}{\xi} \quad (3.9)$$

Where ξ is the *Battery's specific energy* expressed in $\frac{\text{Wh}}{\text{kg}}$ the energy has been calculated with reference to the formula equation 3.8, meanwhile ξ is chosen from the data sheet of a Li-Po S4 battery,

2. **Propeller mass** (m_p) is obtained once the radius of the blades is fixed. Exploiting the relationship derived from statistical data shown in figure 3.3,

$$m_p = 1.8859 \cdot r^2 - 0.7609 \cdot r + 0.1009 \quad (3.10)$$

3. **Body mass** (m_c) is composed of the mass battery plus a possible mass of the payload system with thermal coatings. As a first approximation, it has been estimated that the battery constitutes 50% of the weight of the central body, therefore:

$$m_c = 2 \cdot m_b \quad (3.11)$$

4. **Motor mass** (m_m) is calculated by analysing the datasheets of various motors and deriving a formula linking thrust and weight:

$$m_m = 0.2751 \cdot T_{rot} + 0.0346 \quad (3.12)$$

Total mass is equal to:

$$m = m_c + m_p + m_m \quad (3.13)$$

The calculation of inertia inevitably passes through that of mass. It would be, in fact, impossible to know it without the latter. It depends, moreover, from the geometry and therefore also from the mass distribution. Realize a detailed model in a preliminary phase is a particularly complicated task. For this reason, in this work a basic model is presented in which the central body is schematized by a cube of side l and the rotors with their motors by 4 flat discs with uniformly distributed mass, each one has a diameter equal to the rotor's diameter.

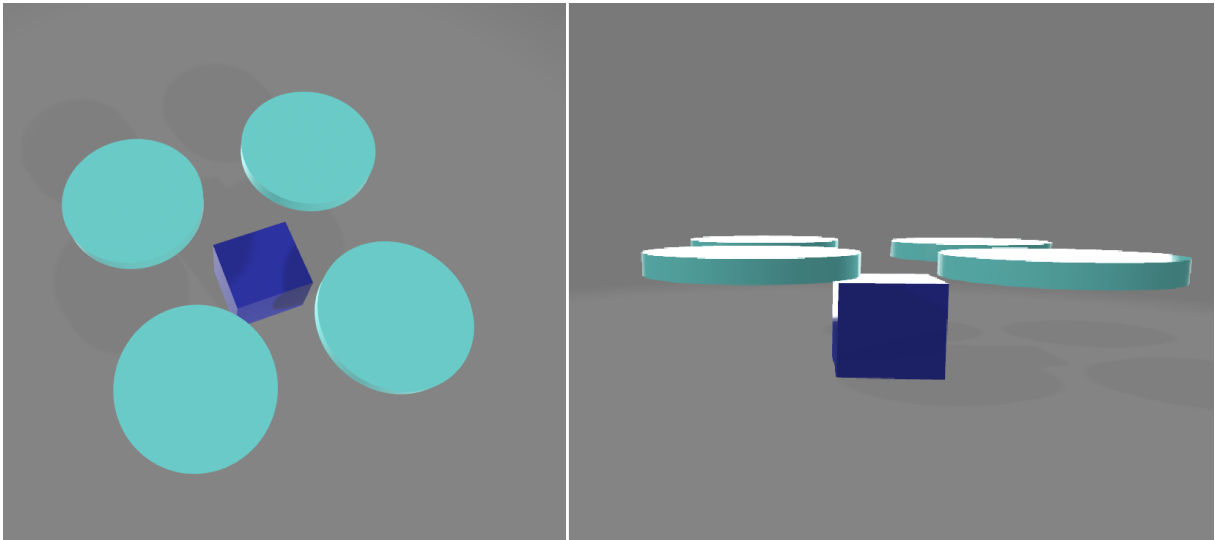


Figure 3.4: Drone inertia model outline

Thus, 2 main contributions to total inertia should be calculated.

- **Rotor's inertia:**

$$\begin{aligned}
 Jx_r &= \frac{1}{4} \cdot m_{rotor} \cdot r^2 \\
 Jy_r &= Jx_r \\
 Jz_r &= \frac{1}{2} \cdot m_{rotor} \cdot r^2
 \end{aligned} \tag{3.14}$$

- **Body inertia:**

$$\begin{aligned}
 Jx_c &= \frac{1}{6} \cdot m_c \cdot (l)^2 \\
 Jy_c &= Jx_c \\
 Jz_c &= Jx_c
 \end{aligned} \tag{3.15}$$

Obviously, the contribution of the rotors must be multiplied by 4 and cannot simply be added to the inertia of the body: the transport moment must be considered. In order to do this, it has been assumed that the drone is perfectly symmetrical and the mass distribution is uniform. So the **Total inertia** is equal to:

$$\begin{aligned}
 Jxx &= 4 \cdot (m_{rotor} \cdot (L^2 + h^2) + Jx_r) + Jx_c \\
 Jyy &= 4 \cdot (m_{rotor} \cdot (L^2 + h^2) + Jy_r) + Jy_c \\
 Jzz &= 4 \cdot (m_{rotor} \cdot 2L^2 + Jz_r) + Jz_c
 \end{aligned} \tag{3.16}$$

Where L is the distance between two adjacent rotors and h is the distance between the rotor's CoM and central body's CoM.

The major inertia component derives from the rotors. Since the vehicle has a symmetry with respect to the XZ plane, the components J_{xy} and J_{yz} of the inertia products are zero and the tensor is presented in the form described below.

$$J = \begin{bmatrix} J_{xx} & 0 & 0 \\ 0 & J_{yy} & 0 \\ 0 & 0 & J_{zz} \end{bmatrix} \tag{3.17}$$

3.1.4 Iterative loop

The elements presented so far are dependent on each other. An iterative loop is used to define them completely.

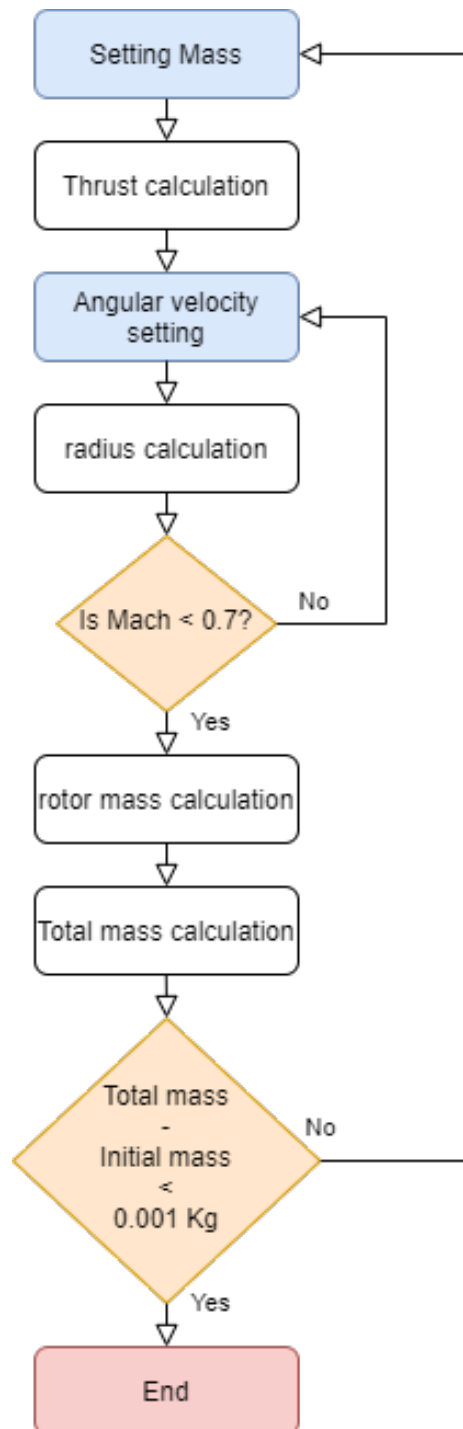


Figure 3.5: Drone's mass calculation flowchart

First, a hypothetical mass that the drone could have as a whole is selected. The thrust is calculated so that it is twice the weight force of the drone:

$$T = \frac{mg \cdot K_{T/W}}{n_{rot}} \quad (3.18)$$

Where n_{rot} is the number of rotors and $K_{T/W} = 2$ is the *Thrust to Weight ratio*.

Then proceed to calculate the radius using the equation 3.1 in which the angular speed n is chosen within a certain operating range of classical propellers so that it is the maximum angular speed possible but at the tip presents Mach less than 0.7. This gives the minimum radius that meets this objective. After this first inner loop, the weight of the propeller is calculated using formula 3.10, the weight of the motor and the weight of the battery, both selected according to the maximum power required. In the case of the motor, formula 3.12 is used, while for the battery reference is made to its specific energy using formula 3.9. At this point the total mass is calculated using formula 3.13. If the error between the mass initially estimated and the mass obtained from equation 3.13 is greater than a certain threshold, the cycle starts again, otherwise the physical and geometric model of the drone is defined and the inertia tensor involved can be calculated.

Table 3.6: Drone configuration parameters

Mass	1.28 kg
arm length	0.72 m
Max angular velocity	3636 RPM
J_{xx}	0,2514 kgm^2
J_{yy}	0,2514 kgm^2
J_{zz}	0,4961 kgm^2

3.2 Guidance and Control

For a feasibility analysis, the system must be able to perform certain maneuvers. So, the drone should follow a path and reach some waypoints. The controller performs this role by analyzing the states (position velocity attitude and angular velocity) in such a way that the assigned target is reached while maintaining stability and avoiding behaviors that would compromise the success of the mission.

In the next sections the models of the guide and the controller are presented.

3.2.1 Guidance algorithm

Creating a guidance algorithm is a very complex task, the drone should follow specific waypoints. Following this idea it has been decided to realize a point tracker.

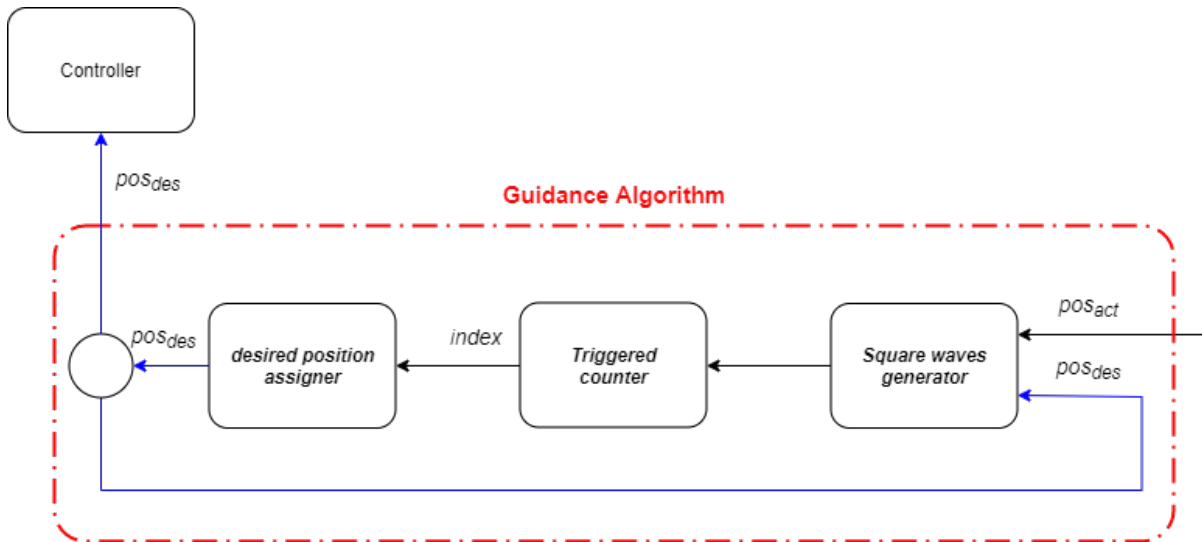


Figure 3.6: Guidance algorithm structure

First, the desired position pos_{des} is compared with the current position pos_{act} , that comes from the sensors and can therefore be affected by errors, which, in this case, have been modeled as arising from the wind. The difference between these two factors is the input signal for the *Square wave generator*: if the difference is less than a certain threshold (i.e. how precisely the desired position is to be reached) the output signal is equal to 1, vice versa it is equal to 0. Then the **Triggered counter** increments a index only if it detects a *rising edge* condition.

The structure of the counter is very simple, as shown in figure ?? each time the *trigger* is activated the counter starts and the sum is then incremented by one. Effectively at each step the sum should reach infinity triggering an algebraic loop, this does not happen thanks to the block *memory* which applies a one integration step delay.

All desired positions are included in an array, which has a point in each row. So finally, the counter indicates which row of the matrix should be read.

The new vector containing the three coordinates of the new desired position is given to the controller. The figure 3.7 represents the inputs of each of the three blocks represented above. The error between the desired and actual position is shown in green. It decreases with the approach of the drone to the target, however, as soon as the target changes it increases instantaneously. This occurs at the peaks on the blue curve in 3.8. This is the quadratic function mentioned before, which returns the unit value when the error in position is less than a certain threshold. Zooming in shows how the function is actually a square wave. These graphs also provide important information about the time it takes to reach a specific goal. Even changing the concavity of the error curves provides data. It is due to the reduction of speed by the controller, this causes a slowing down in the decrease of the value of the function itself which leads to a delay in achieving the target. Reaching a waypoint, in fact, does not imply just passing it, but keeping its position. An abrupt arrival may not satisfy this condition, for this reason some measures have been taken that will be described in the next paragraph.

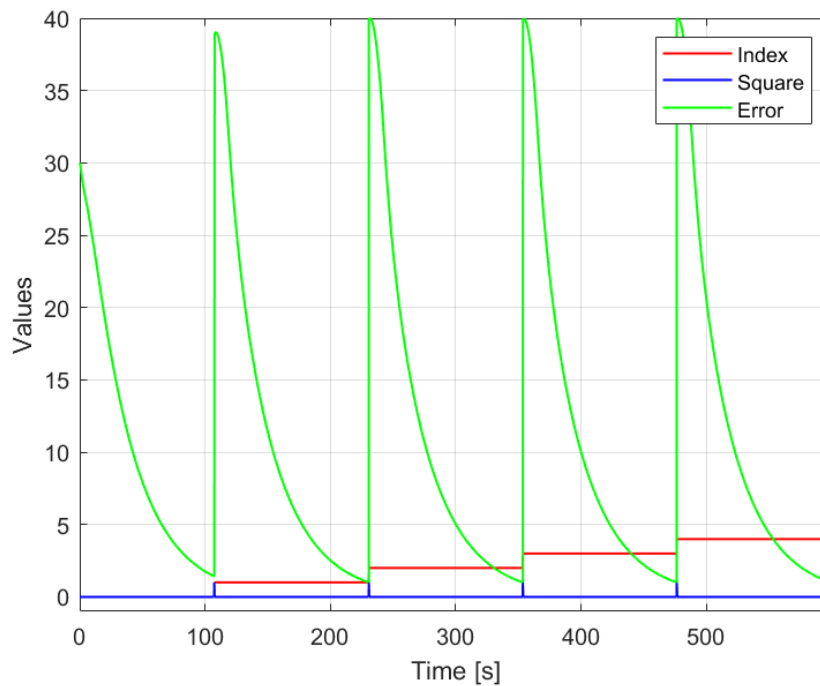


Figure 3.7: Principal Guidance algorithm's parameters

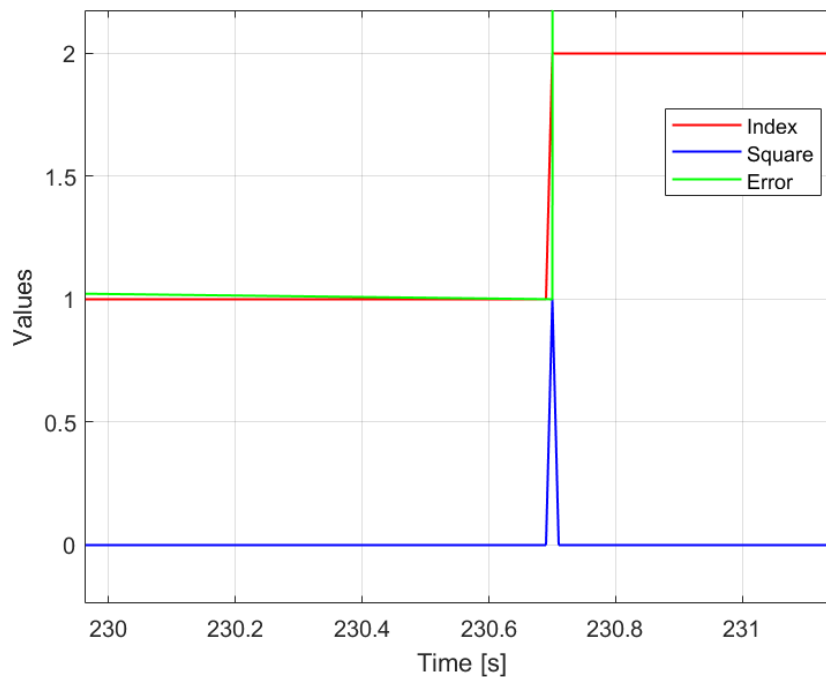


Figure 3.8: Counter and square waves generator

3.2.2 Control design

Control theory deals with the analysis and synthesis of logic for the control of a system. In the broadest sense, a system can be thought of as a collection of components or parts that work together to perform a particular function [25]. A control system can be classified in:

- *Open-Loop control systems* that work receiving an input that indicates to the system how it must act, the output is a command that does not influence in some way the input to the successive step of integration,
- *Closed-Loop control systems* that are also called *Feedback control systems* because they link the output to the input through a signal that modifies the input itself.

For the type of mission analyzed in this work, it is essential to use the feedback control system because it is the most accurate; to remove it, realizing an open-loop control system, would mean to make a hardware without sensors, in which there is no possibility to know the current status and the commands would be generated a priori.

Generally, in feedback control systems, the output signal is compared with the input signal, resulting in an error that is the main control variable for the *forward path elements*.

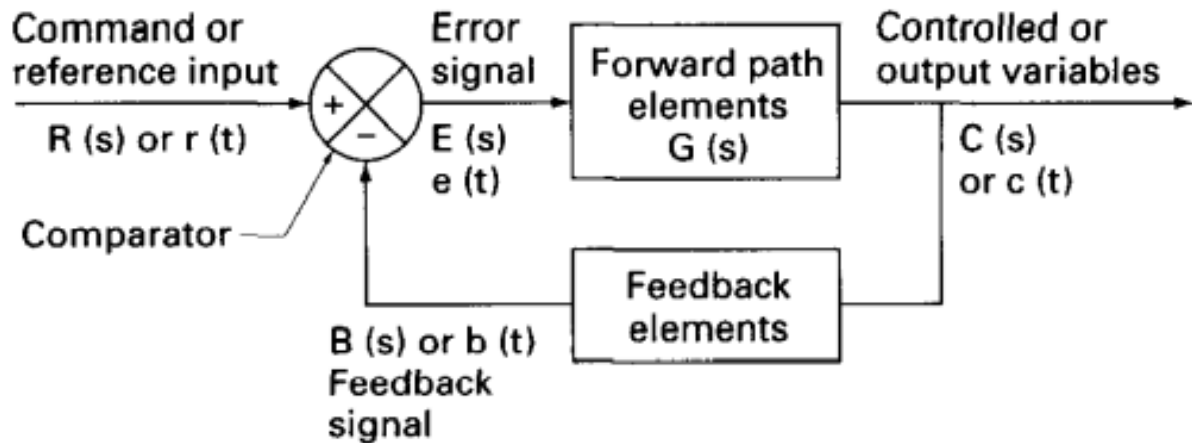


Figure 3.9: Controller typical structure [25]

Each component of the control system is defined in terms of its transfer function that is defined as the ratio of the Laplace transform of the output to the Laplace transform of the input where the initial conditions are to be known [25].

$$T.F = \frac{\text{Laplace transform of the output}}{\text{Laplace transform of the input}} \quad (3.19)$$

The symbols used in the block diagram are defined as follows:

- **R(s)** Reference input,
- **C(s)** Output signal (variable to be controlled),
- **B(s)** Feedback signal,
- **E(s)** Error or actuating signal,
- **G(s)** $C(s)/E(s)$ forward path or open-loop transfer function.

However, feedback in itself does not ensure that the system will be stable. Therefore, to design a feedback control system one needs analysis tools that allow the designer to select system parameters so that the system will be stable.

The type of control chosen to test the drone is the PID, it develops the command based on the error and its trend; in fact it applies three operations to the error that are then overlapped:

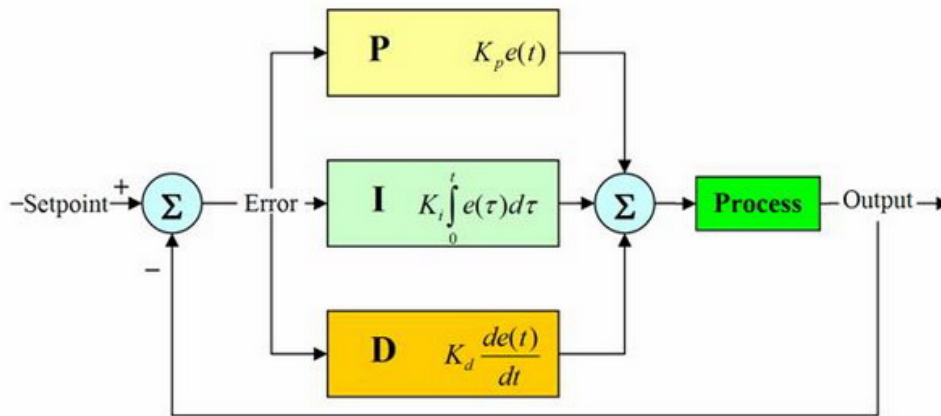


Figure 3.10: PID controller basic structure

- *Proportional* that provides a command proportional (k_p) to the error, it allows to quickly bring the system to the values of regime, however it renders the system unstable causing oscillations in the around of the desired one,
- *Integrative* that integrates the error using an accumulator, which is then multiplied by an appropriate gain, this type of operation allows to correct the error at steady state, but as the proportional controller makes the system unstable,

$$\eta(t) = k_i \int_0^t e(t) dt \quad \text{or} \quad \eta(s) = \frac{k_i}{s} e(s) \quad (3.20)$$

- *Derivative* that consists in applying an anticipatory filter able to correct steady-state instabilities, this is the main advantage of the latter component of the PID, however, this comes at a cost in terms of steady-state reach time, *rising time*, which could become excessively long. In addition, this type of filter is particularly subject to errors, since it depends on the derivative of the error. For this reason also in this case it is advisable to set a suitable gain multiplier or adopting particular solution as described below.

$$\eta(t) = k_d \frac{de}{dt} \quad \text{or} \quad \eta(s) = k_d s e(s) \quad (3.21)$$

Adding up all three effects it is possible to reduce the disturbances of the single ones obtaining a quite effective controller [25].

$$u(t) = k_p e(t) + k_i \int_0^t e(t) dt + k_d \frac{de(t)}{dt} \quad (3.22)$$

There are four variables to be controlled (position, velocity, attitude and angular velocity) so four controllers are required. The motion of the drone, however, makes them interdependent making often necessary a cascade architecture: within it each PID controls a variable and the error that it receives is nothing more than the output of a previous one, except for the top that has as input directly the position error.

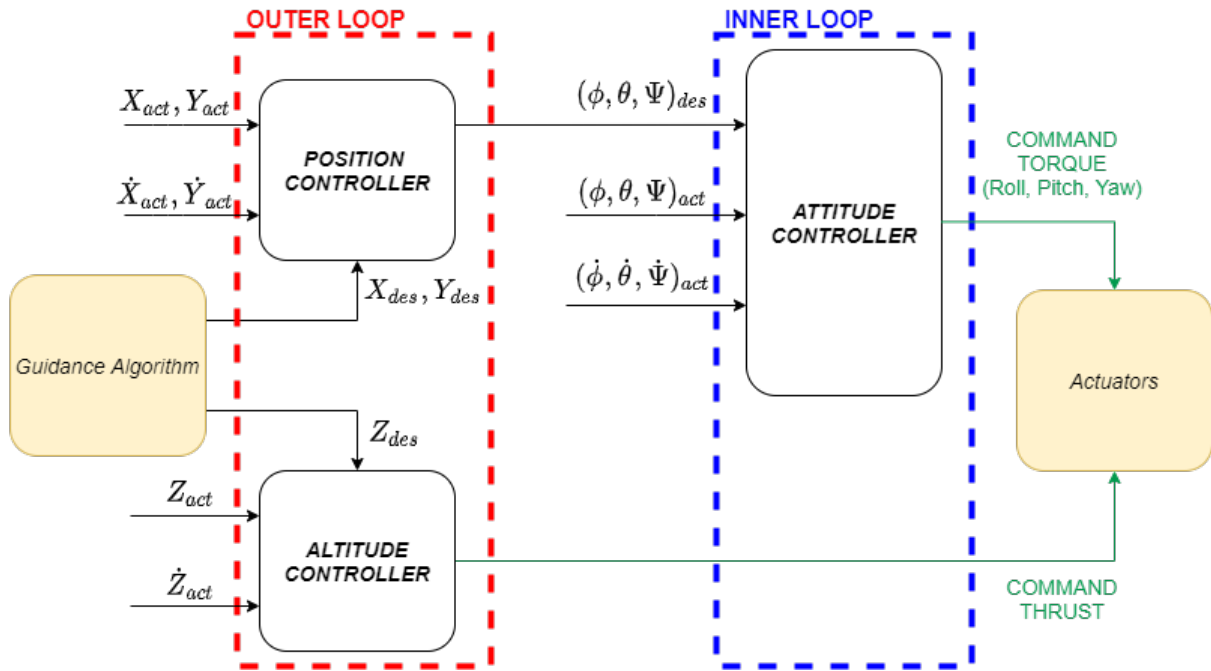


Figure 3.11: Cascade controller structure

Position and velocity controllers are located in the outer loop, while attitude and angular velocity in the inner loop. This architecture has several advantages, like the possibility of linking the attitude to the translation of the drone so as not to have undesired behaviors.

Outer-Loop

The outer loop is responsible of position and speed control. It inside has:

- **Position controller** that generates the desired settings taking into account the positions and speeds in the X-Y plane. In particular, θ and ϕ controller have the same structure, while ψ controller has a different one.

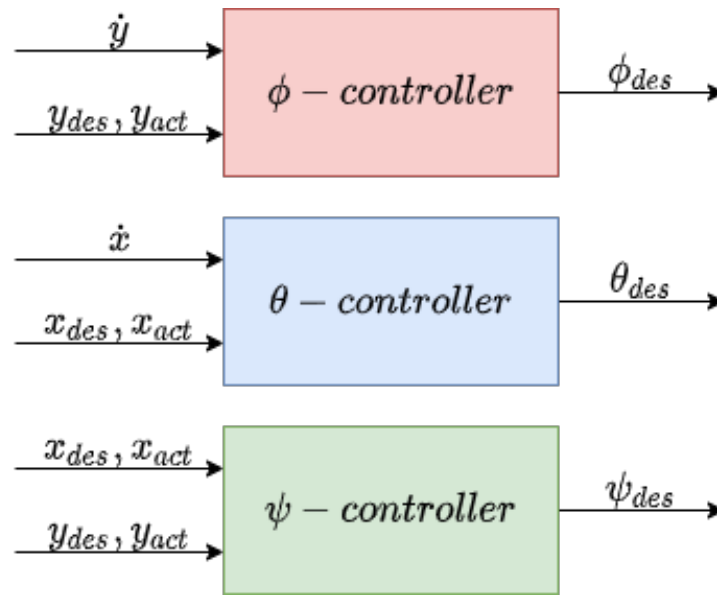


Figure 3.12: Position controller structure

The first one uses the position difference to generate a speed command. Therefore, the speed is the real control parameter of the PID. Its error, in fact, is integrated, differentiated and multiplied proportionally through appropriate gains. What this block actually performs is a *speed follower*.

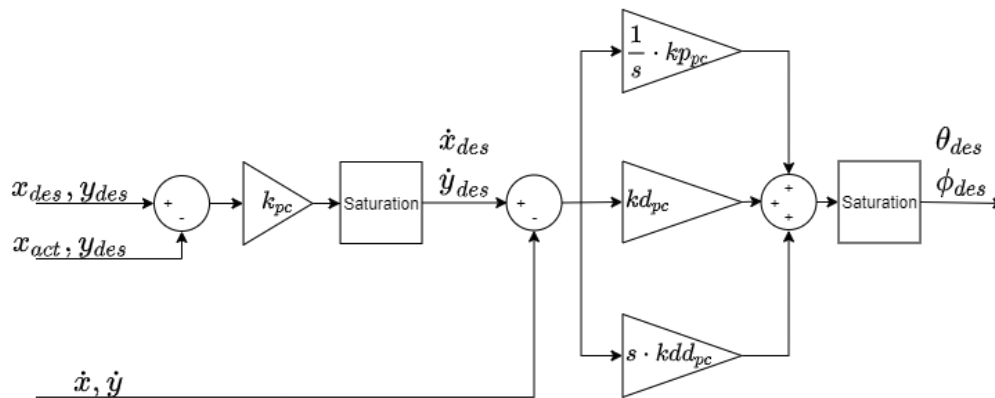


Figure 3.13: θ and ϕ controller

The main disadvantage of the structure is therefore highlighted here. In fact, in case the position errors are too big, this would heavily influence the speed to chase which would be high and proportional to the distance. For this reason saturation blocks are adopted. Beyond a certain value, these, act as limiters, inhibiting the previous behaviors to them and transforming what comes before in constant values. Saturation blocks are scattered throughout the control chain as the interdependence link between position and velocity is repeated between one variable and its next along the chain.

However, this is not the only type of saturation adopted. Another typical drawback of having an integrator inside the PID is the phenomenon called *wind-up*: If the tracker did not reach the desired speed for a certain period of time, an error would accumulate inside the integrator, if the command of the same would decrease, the drone would not decelerate because the accumulated error would prevent it from doing so. For this reason the integrators are saturated, but in a different way than the other variables, what is done is not to limit the output but the possibility of accumulating error inherent in the same. On the other hand there is the ψ controller which has a simpler structure: it takes the current and desired points and from it calculates the yaw angle needed for the x-axis body to align with the conjunction between the two points.

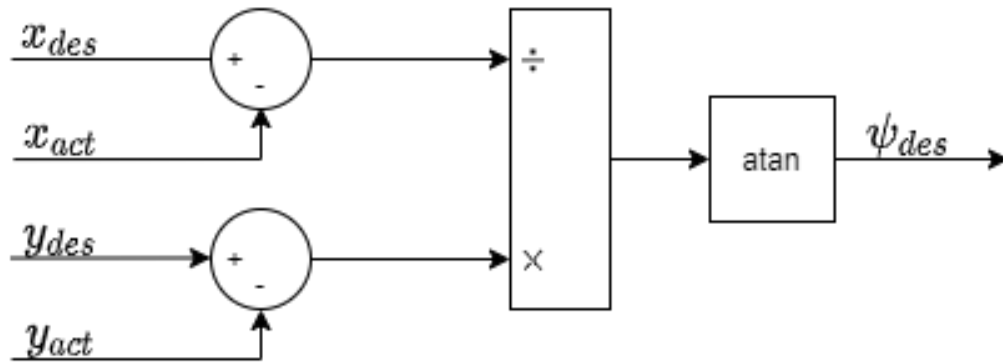


Figure 3.14: ψ controller

- **Altitude controller** has the same configuration as the θ and ϕ controllers but with the variables referenced to the z-axis. Thanks to it what is obtained, is not a desired attitude command like the previous blocks, but directly a thrust command. It's important to specify that the generated thrust is the one needed for the drone to maintain the height established with $\theta = 0$ and $\phi = 0$. But the attitude variations decrease the lift projection along the D-axis of the NED system compared to the hovering condition. This leads to a very small loss of altitude when the aerobot changes direction. However, they last only a few moments at low attitude such that the controller can immediately provide a thrust command.

Inner-Loop

The inner loop is responsible of attitude and angular velocity control. It inside has the *Attitude controller*. First, the desired attitude is rotated by exploiting rotation matrix number 3 of the equation 2.9 that refers to the yaw. The position controller, in fact, generates an attitude in θ and ψ that considers the x body-axis of the drone perfectly aligned with the conjunction between the

current point and the desired waypoint. It is therefore necessary to consider the misalignment due to the yaw angle of the drone and rotate the input so that the commanded attitude takes this into account.

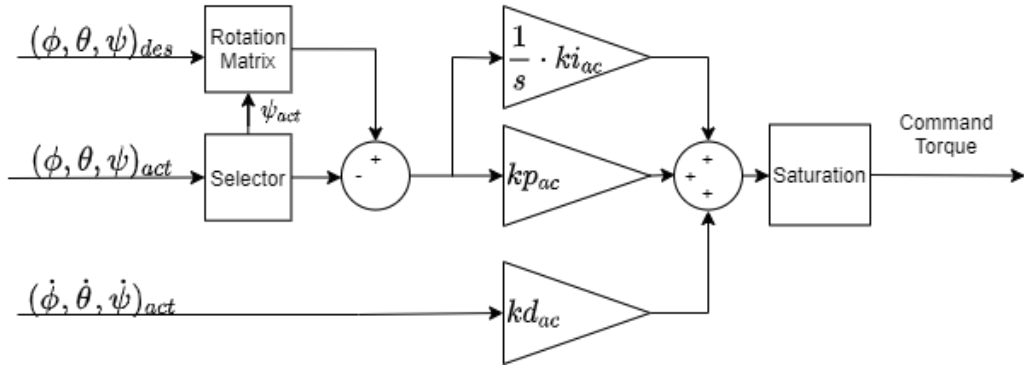


Figure 3.15: Attitude controller

The rest of the structure is very similar to the θ and ϕ controllers but the derivative term is calculated using the angular velocities directly, in this way the discontinuity in $r(t)$ will be still transferred through proportional into control signal, but it will not have so strong effect as if it was amplified by derivative element [26]. The output is the control torque that must be applied to perform certain maneuvers.

3.3 Actuators

The components of the command enter inside the actuation, this provides that the command signals are transformed into voltage by a special *Motor Mixer*. The voltage, within the motor's electrical circuit, provides a current that sets the propellers in motion. Therefore, the current is proportional to the voltage, which in turn depends on the command. What actually happens to the system is a dual delay due to the electronics of the *Motor Mixer* and the actuation time of the mechanical part of the motors due to its inertia. Modeling the *Motor Mixer*, however, is a choice that leads to the subsequent development of hardware and therefore could be costly. In the present work, it is not modeled, but these delays were added via special functions to account for them.

4. Test and results

Once the flight simulator has been developed, in order to complete the feasibility analysis, several maneuvers must be carried out to allow conclusions to be drawn regarding the reliability of the guidance and, above all, the adopted control. For each of them, the states are analysed and factors such as the accuracy in reaching a specific waypoint, the ability to reach certain speeds, the stability of the attitude and thus also the resulting oscillations are discussed. Tests are conducted both in the presence and absence of wind in order to evaluate the response to a typical disturbance on Mars. In fact, the wind disturbs the sensors when detecting speed, providing the controller with an error-affected measurement that, due to its architecture, inevitably leads to a drop in performance. To highlight these effects, different maneuvers are discussed in the following paragraphs; specifically, the first two maneuvers are used to understand how the drone responds to the request to maintain a specific point in space or to reach a predefined one, while the other is composed of a series of waypoints. The main difference is that in the latter case, for each point reached, errors accumulate due to inaccuracy, and between one waypoint and another the conditions are not perfectly stationary, so it's possible to see how the system reacts once the next target has been acquired.

4.1 Hovering

Hovering is a particular type of flight that occurs when the drone is stationary in the air at zero speed and constant altitude. In this case, one speaks of stationary flight or point flight, as the drone's course in space indicates a simple point. The hovering function is ideal for taking photos that are not blurred. In the generic case let's assume that the drone is at a height of 10 metres with $\theta = 0$ and $\psi = 0$ and let's run the simulation for a certain time interval. In the absence of wind, the drone maintains its position perfectly without oscillating. The starting position is $pos = \begin{bmatrix} 0, 0, -10 \end{bmatrix}^T$ and the desired one is the same, while all the initial velocities are null. Note that the negative value along the D axis is due to the reference system and indicates how high the drone is above the ground. During this condition all the four propellers turn at the same speed and produce the same thrust. Note that initially the drone loses a few centimetres of altitude, this problem is related to the fact that the simulator does not have initial conditions regarding the rotation speed of the propellers or the thrust. For a few steps of integration the system falls under the effect of gravity, until the controller activates the thrust command. To overcome this problem, subsequent simulations are carried out by always taking off from the ground.

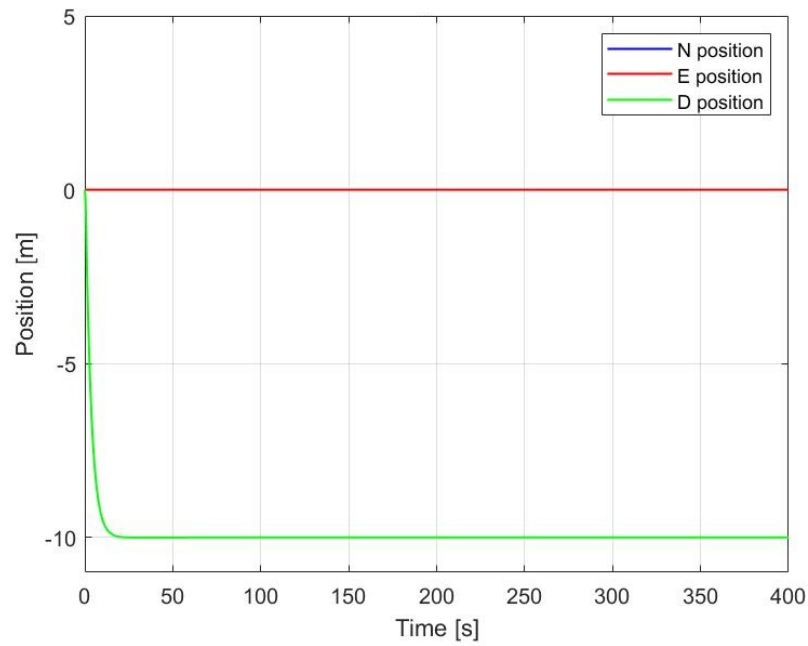


Figure 4.1: Evolution of position in Hovering condition

In the case of wind presence there are slightly different results.

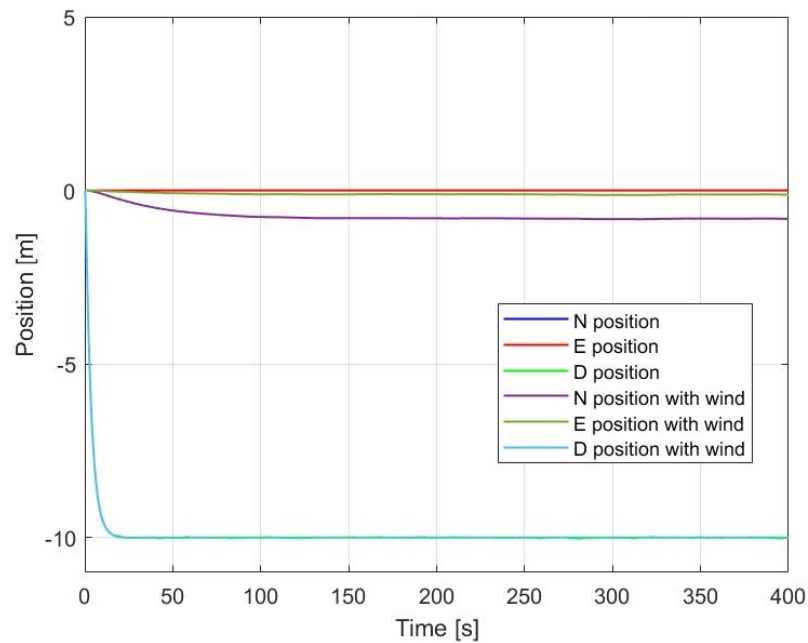
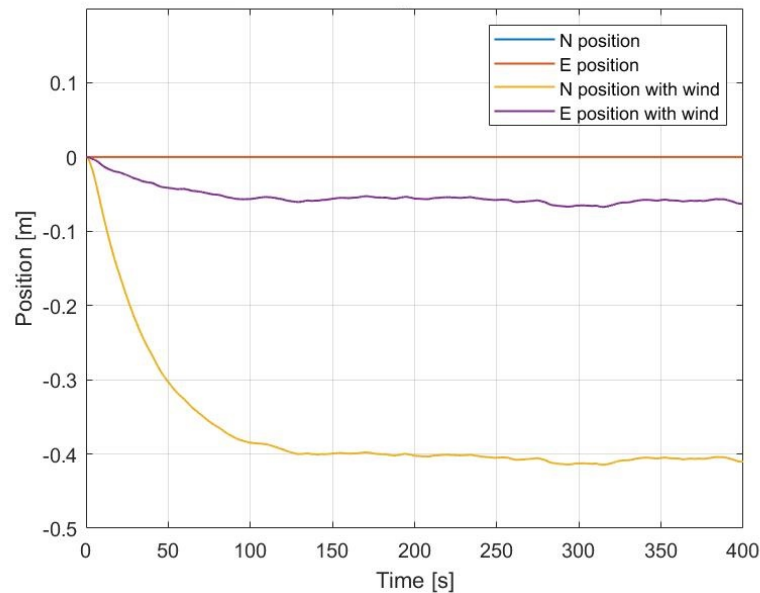


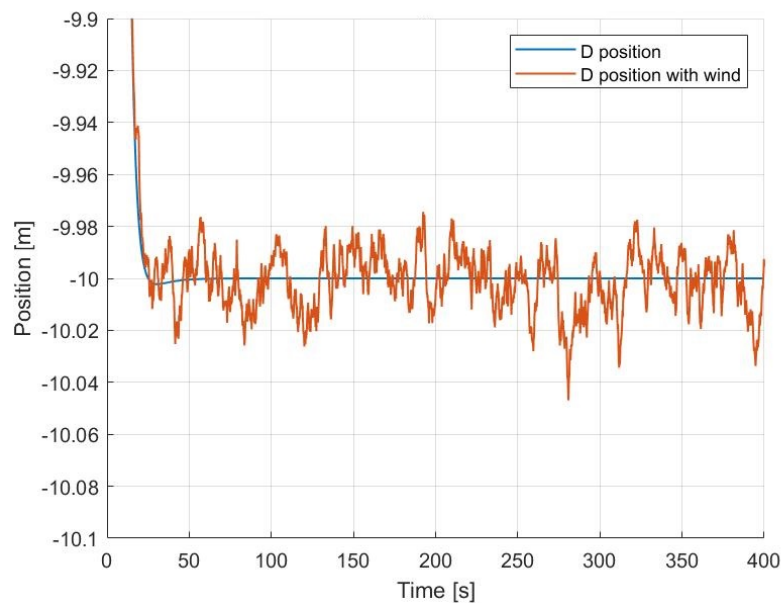
Figure 4.2: Evolution of position in Hovering condition with wind

As can be seen from the graph 4.2 after an initial transient the final position taken is quite different. It is observed that the drone oscillates along the Down direction by about 5 cm, while

the biggest error is in the North direction, which is also the axis where the wind intensity is greatest. The controller is unable to settle at the exact desired point. The wind in fact interferes with the sensors that provide the controller with different speeds with respect to the NED system and the difference between the two values is proportional to the amplitude of the disturbance.



(a) Error in North and East direction

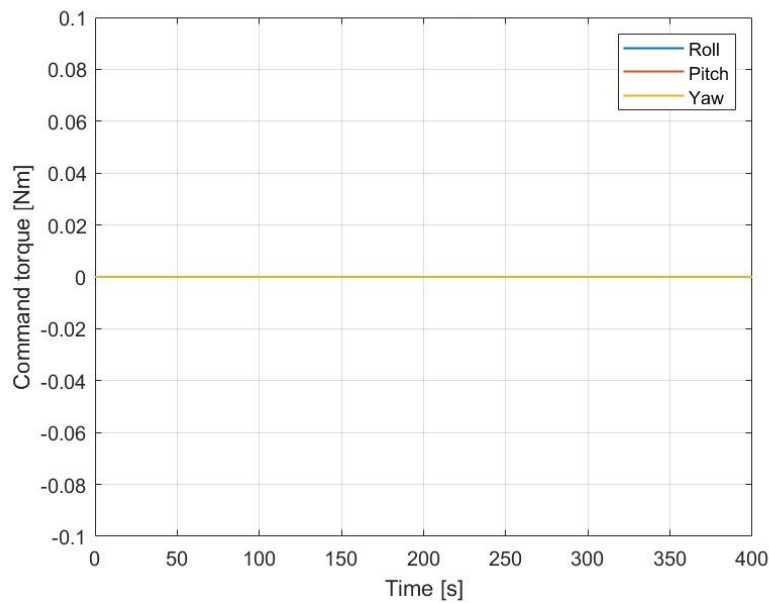


(b) Error in Down direction

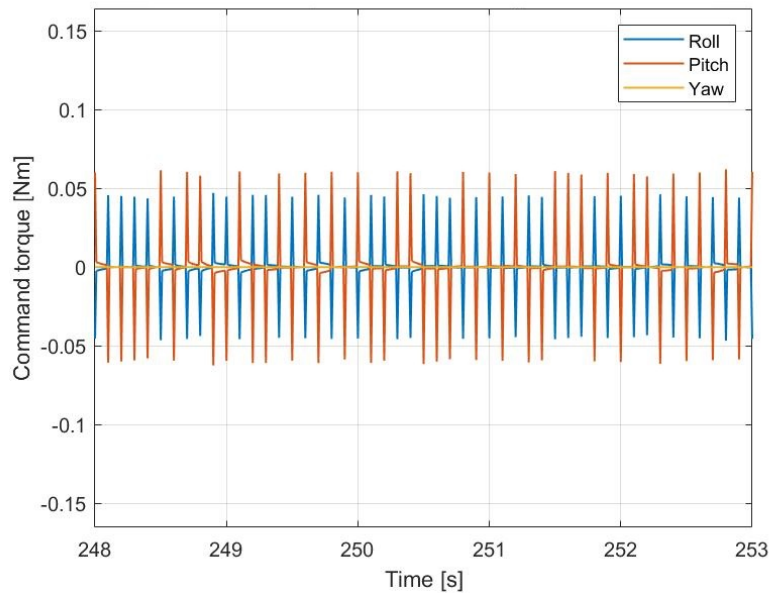
Figure 4.3: Error caused by wind during Hovering maneuver

At beginning of the simulations the drone is actually stationary with respect to the ground

so the position control returns a desired speed of zero (see figure 3.13), however the sensors register a movement of the system caused by the wind. The difference between these two signals then generates a command that causes the error shown in the graphs. As expected, the control is in fact oscillatory and fails to dampen its effect, which also has an impact on the attitude.



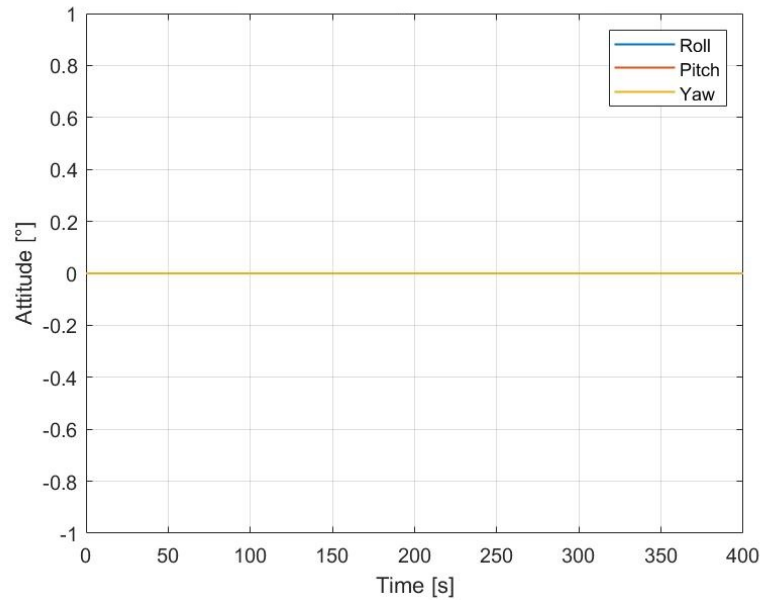
(a) Command torque



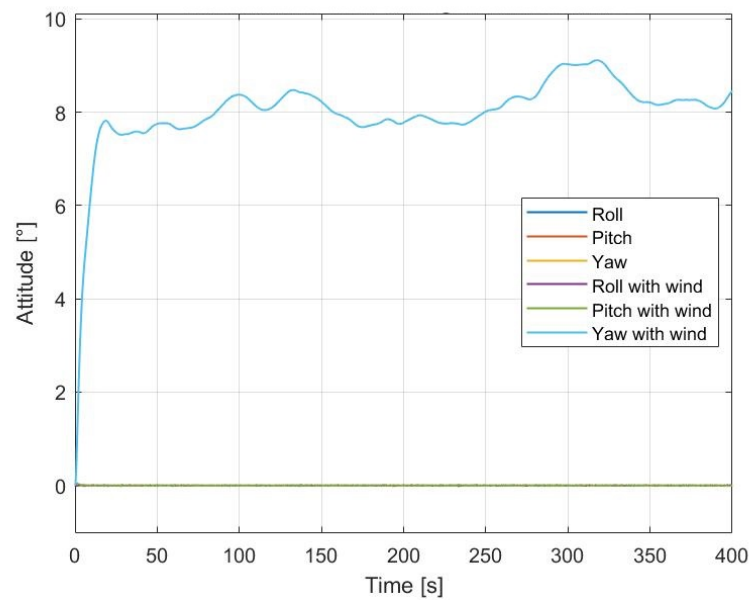
(b) Command torque with wind

Figure 4.4: Effect of errors on command torque

The greatest effect, as can be seen, is felt in the yaw angle, which oscillates around values of eight degrees during gusts, whereas in the nominal condition it should be zero. This is due to the controller's calculation of the desired yaw angle. It depends on the ratio of position errors in the N-E plane.



(a) Without wind



(b) With wind

Figure 4.5: Attitude angles during Hovering maneuver

4.2 Simple translation

This maneuver involves reaching a point from zero altitude and arriving at only one specific waypoint, which is then maintained over time. In particular it was chosen to reach point $\begin{bmatrix} 100, 100, -10 \end{bmatrix}^T$ in order to move in all three directions.

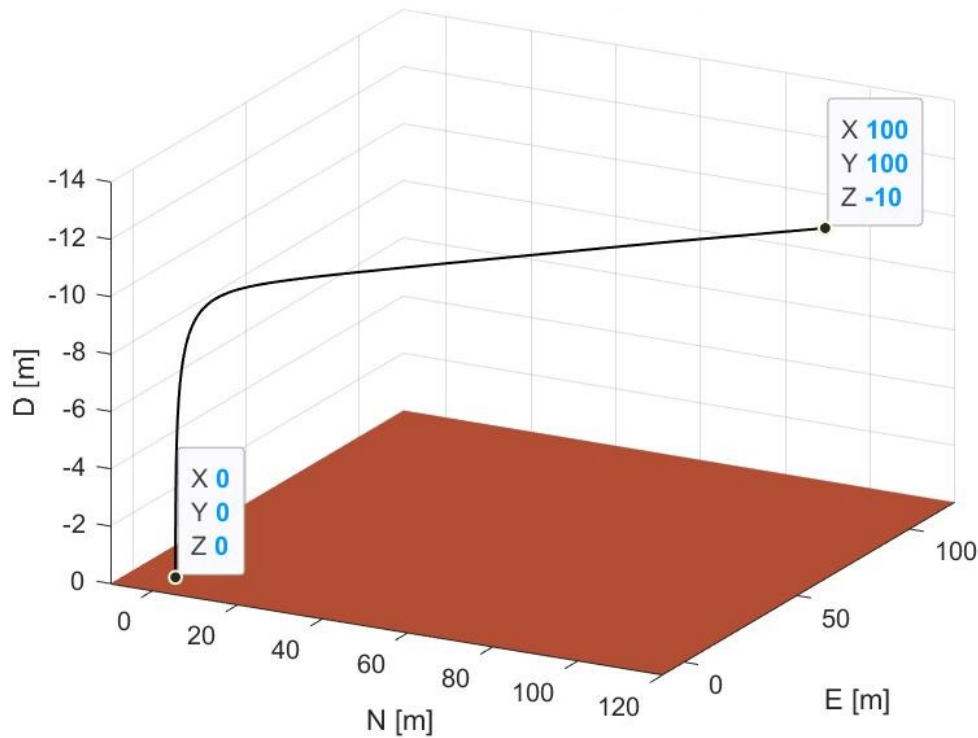


Figure 4.6: Trajectory of the drone in Simple translation maneuver

The drone must reach a point whose coordinates are equidistant in each axis. As can be clearly seen from the graph 4.11, in the absence of wind, the movement along the N-E plane takes place on the bisector, because the drone moves equally along both the N and E axes. However, the thrust component that allows translation along this plane is always less than that which pushes it along the D axis. The thrust generated by the drone, obviously, is always directed towards the z-body axis, what changes is the projection of the force on the three axes of the NED system. This effect strongly depends on the attitude of the drone, but in order to guarantee its stability it cannot exceed certain thresholds, which translates into the system's ability to move much faster along the D axis than in the other two.

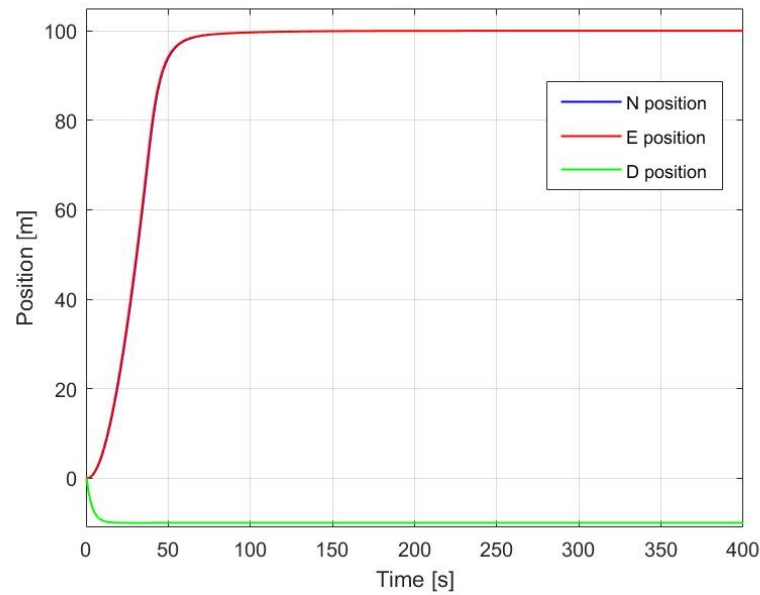


Figure 4.7: Evolution of position in Simple translation maneuver

The graph 4.7 also shows a change in the slope of the curve near the end point. This suggests looking at the speed graph. Also in this case, the velocities relative to the N and E axis are superimposed, and all three derivatives are first increasing (in modulus) and then decreasing. This explains the change in concavity.

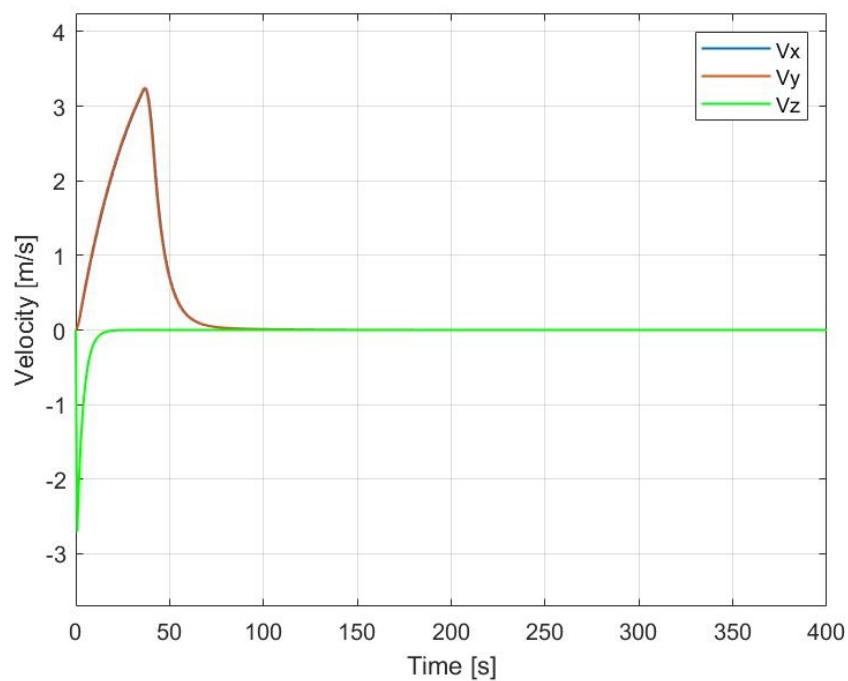


Figure 4.8: Evolution of velocities in Simple translation maneuver

From a physical point of view, the trend of the derivative is explained by the controller. In the initial phase, commands are given to change the attitude abruptly. The drone advances towards the target and the position error gradually decreases. This causes the command to be lowered and therefore the acceleration of the drone to decrease. When the desired point is close enough, the controller starts to command an opposite acceleration which implies lower speeds than those required. At that point, the command is reversed. This generates the peak in speed that it's possible to see in the graph 4.8. However, if during the path the drone acquires speeds greater than a certain threshold, instead of the peak there will be a constant line that will then decrease again once it is close to the finish line.

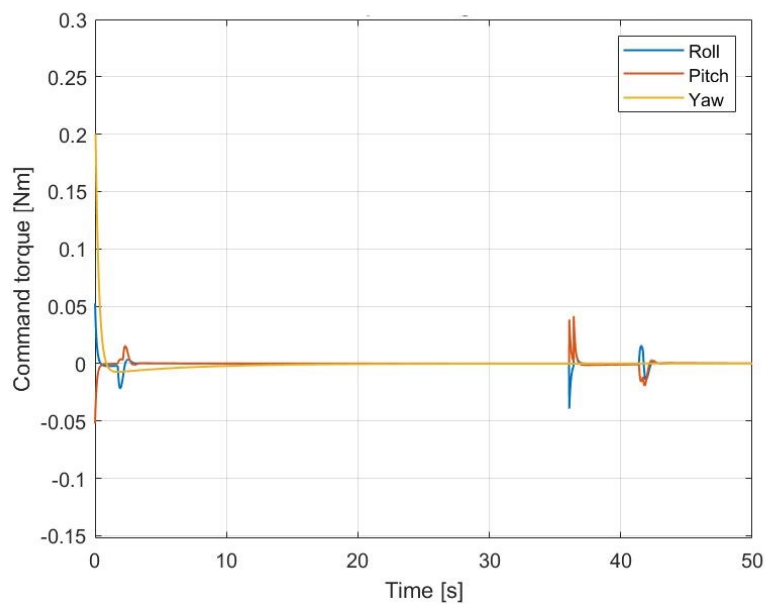


Figure 4.9: Command torque during Simple Translation maneuver

The maneuver changes in the presence of wind, as in the previous case the biggest errors reside along the N axis. However, the errors in position remain similar to those of the previous maneuver. The real problem is in the attitude; in fact, the fluctuations are greater than in the previous case, causing even greater errors in yaw angle as can be seen in 4.11.

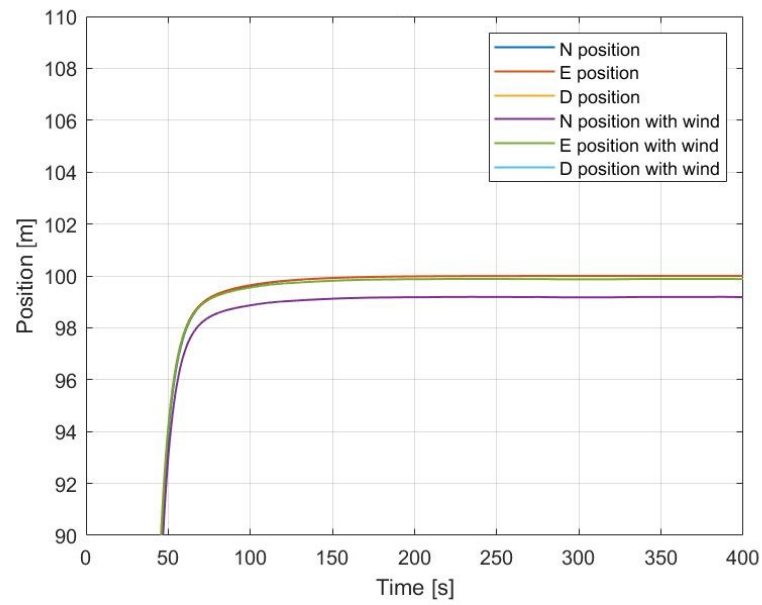


Figure 4.10: Position errors caused by wind in Simple Translation maneuver

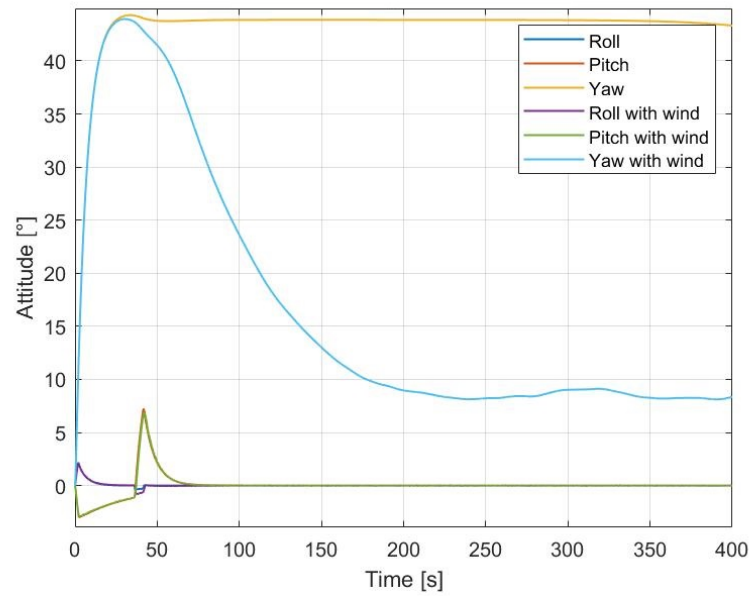


Figure 4.11: Attitude errors caused by wind in Simple Translation maneuver

4.3 Square maneuver

The last maneuver involves reaching several waypoints. The aim is to demonstrate that the position error remains constant despite the accumulation of several desired positions thanks to the appropriate saturations provided in the controller. Starting from zero altitude, the drone reaches a fixed height and reaches the four vertices of a square, describing an area of approximately 400 m^2 .

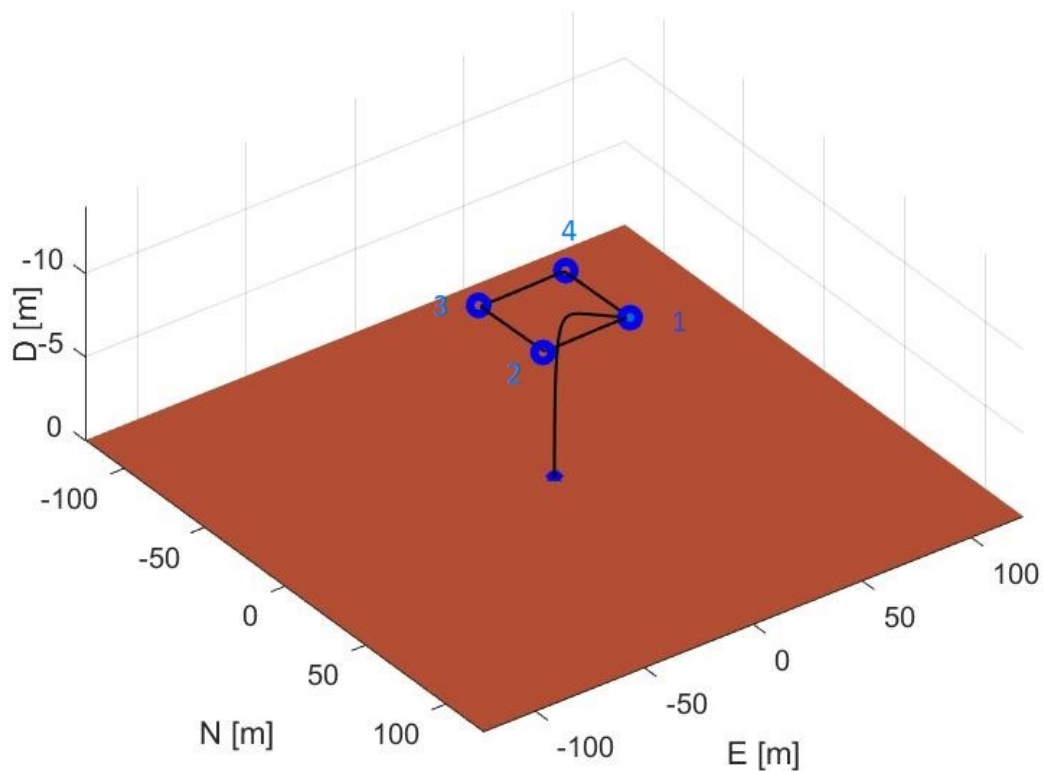


Figure 4.12: Trajectory of the drone in Square maneuver

The system behaves as if it were carrying out a series of simple translations, following all the peculiarities discussed in the previous paragraph. As in the previous case, the drone is able to reach the desired path, with a reduced control effort and with reduced velocity. Moreover, the altitude (which is usually a critical parameter) is maintained constant at the desired value, during all the maneuver. However, it should be pointed out that in windy conditions a lower degree of manoeuvring precision must be required of the system. If this were not the case, the aerobot would try in vain to reach a given waypoint, ignoring the presence of the wind. The case illustrated in the figure 4.14 describes just such a situation, in which the counter is not

incremented and the next waypoint is not read because the minimum proximity condition is never satisfied.

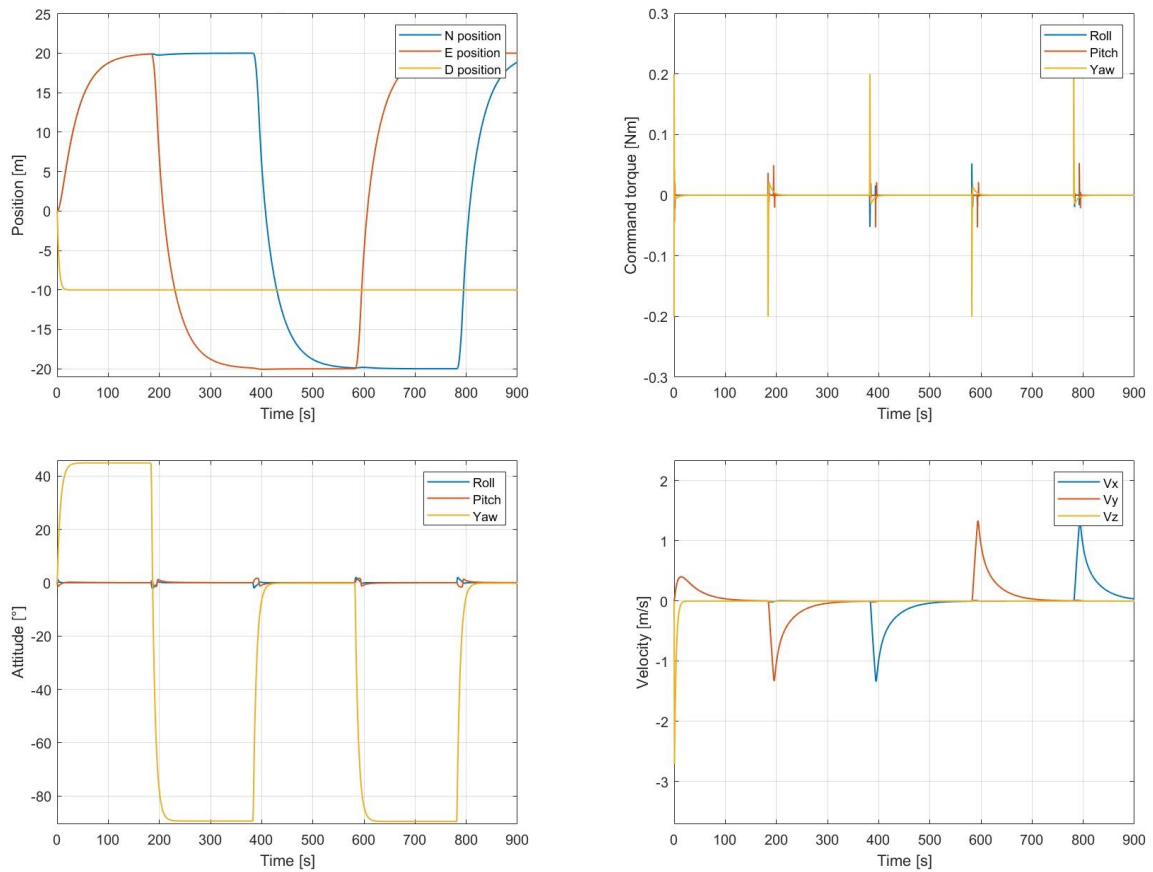


Figure 4.13: Output of Square pattern

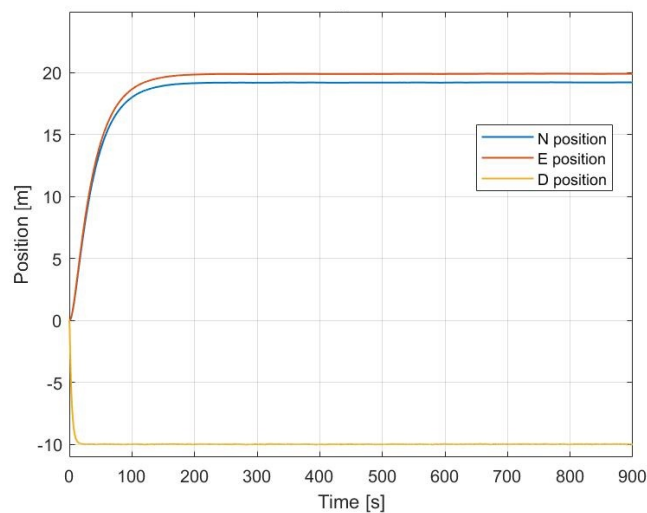


Figure 4.14: Maneuver failure in windy condition

5. Conclusions & Open points

In this thesis, a simulation model of a quadrotor drone in a martian environment is presented. The aim is to carry out a feasibility study on the possibility of a flight to Mars and the potential and maneuvering capabilities of these systems. It has therefore been equipped with a guidance algorithm and a special controller to perform the maneuvers. In particular, a cascade architecture by a sequence of PID controllers has been chosen. By carrying out simulations in Matlab/Simulink, different configurations can be tested by tuning the controller parameters. With the found values, good results are obtained in terms of trajectory tracking. However, by adding windy conditions, all the limits of the PID controller are shown. In particular, the errors in position with respect to the previous condition increase and the instability continues at the same rate. Nevertheless, these position errors are acceptable for the tasks that a drone is generally required to perform. However, in the case where the drone is used as an image or data acquisition device, so it is assumed to have a payload, more stringent attitude requirements are inevitable. In this case, the PID cannot meet these requirements and is not robust enough to fulfill such tasks. In particular, the sudden change of state values, combined with wind disturbance, does not allow the controller to achieve a fluctuation-free condition.

The work therefore has several open points that can lead to a considerable improvement in results:

- **Implementing others controllers** is certainly one of the key points for future work. The choice could be for a Sliding mode controller to ensure higher stability, in this way the system would be able to acquire data by eliminating noise due to oscillations.
- Much **more accurate disturbance models** would allow finer parameter tuning. The main noise, in fact, is the modelled wind as explained in the paragraph 2.5. However, the wind oscillates around predefined values on each axis and stays in a certain circle; because of this, it always blows stronger in one direction. This is obviously a limitation of the model.
- **Model the actuators** by entering the equations governing the operation of the Electronic Speed Controller (ESC) and the mechanical actuation part of the motors. These constitute two disturbances, the first related to the delay time of the Omhico-inductive circuits, the second related to the inertia of the motor. They delay and slightly alternate the command. Including a model of this type would also make it possible to assess the effects of varying the angular speed of the propellers on the system.

- The value of the **thrust coefficients should be calculated experimentally**, but has been found in other laboratory studies, assuming that similar components are used.
- **Implementing an Extend Kalman Filter** would improve controller performance by reducing noise from sensors
- **Try different guidance algorithms**, the current one requires reaching certain waypoints but has no requirement on arrival time. This is a key parameter for this type of mission as flight times can be reduced due to the size of the drone. It is therefore necessary to foresee that the drone can perform all maneuvers and land safely.

Bibliography

- [1] Mostafa Hassanalian, Devyn Rice, and Abdessattar Abdelkefi. Evolution of space drones for planetary exploration: A review. *Progress in Aerospace Sciences*, 97:61–105, 02 2018.
- [2] NASA. Mars helicopter ingenuity fact sheet.
- [3] Anubhav Datta, Beatrice Roget, Daniel Griffiths, Gregory Pugliese, Jayanarayanan Sitaraman, Jinsong Bao, Lin Liu, and Olivier Gamard. Design of a martian autonomous rotary-wing vehicle. *Journal of aircraft*, 40(3):461–472, 2003.
- [4] Pengcheng Wang, Zhihong Man, Zhenwei Cao, Jinchuan Zheng, and Yong Zhao. Dynamics modelling and linear control of quadcopter. In *2016 International Conference on Advanced Mechatronic Systems (ICAMechS)*, pages 498–503. IEEE, 2016.
- [5] Nasa. *Mars Climate Database*.
http://www-mars.lmd.jussieu.fr/mcd_python/.
- [6] Marco B Quadrelli, Aaron Schutte, Jasmine Rimani, and Luca Ermolli. Aero maneuvering dynamics and control for precision landing on titan. In *2019 IEEE Aerospace Conference*, pages 1–16. IEEE, 2019.
- [7] NASA. Mars fact sheet, 2020.
- [8] Robert Braun, Henry Wright, Mark Croom, J. Levine, and David Spencer. Design of the ares mars airplane and mission architecture. *Journal of Spacecraft and Rockets*, 43:1026–1034, 09 2006.
- [9] L. A. Young, E. Aiken, P. Lee, and G. Briggs. Mars rotorcraft: possibilities, limitations, and implications for human/robotic exploration. In *2005 IEEE Aerospace Conference*, pages 300–318, 2005.
- [10] Nathan Scott Collins. *System Design and Nonlinear State-Dependent Riccati Equation Control of an Autonomous Y-4 Tilt-Rotor Aerobot for Martian Exploration*. University of Surrey (United Kingdom), 2016.

-
- [11] Hanbing Song. *A Hybrid Martian VTOL UAV: Design, Dynamics and Control*. University of Surrey (United Kingdom), 2008.
- [12] Wei Shyy, Yongsheng Lian, Jian Tang, Dragos Vieru, and Hao Liu. *Aerodynamics of low Reynolds number flyers*, volume 22. Cambridge University Press Cambridge, 2007.
- [13] Christian Hirt, SJ Claessens, Michael Kuhn, and WE Featherstone. Kilometer-resolution gravity field of mars: Mgm2011. *Planetary and Space Science*, 67(1):147–154, 2012.
- [14] Nasa. *Mars Atmosphere Model*.
<https://www.grc.nasa.gov/www/k-12/airplane/atmosmrm.html>.
- [15] Kanaiya Agrawal and Punit Shrivastav. Multi-rotors: A revolution in unmanned aerial vehicle. *International Journal of Science and Research*, 4(11):1800–1804, 2015.
- [16] Brian L Stevens, Frank L Lewis, and Eric N Johnson. *Aircraft control and simulation: dynamics, controls design, and autonomous systems*. John Wiley & Sons, 2015.
- [17] J. Lingard. Precision aerial delivery seminar ram-air parachute design. 03 2021.
- [18] Giorgio Guglieri Giovan Battista Errante and Ivano Musso. A methodology for the design of a guided parafoil recovery system.
- [19] Damian Toohey. Development of a small parafoil vehicle for precision delivery. 03 2006.
- [20] P. Lissaman and Glen Brown. Apparent mass effects on parafoil dynamics. 02 1993.
- [21] Matteo Scanavino, Arrigo Avi, Andrea Vilardi, and Giorgio Guglieri. Uas testing in low pressure and temperature conditions. In *2020 International Conference on Unmanned Aircraft Systems (ICUAS)*, pages 1757–1765. IEEE, 2020.
- [22] John Brandt and Michael Selig. Propeller performance data at low reynolds numbers. In *49th AIAA Aerospace Sciences Meeting including the New Horizons Forum and Aerospace Exposition*, page 1255, 2011.
- [23] Matteo Scanavino, Andrea Vilardi, and Giorgio Guglieri. An experimental analysis on propeller performance in a climate-controlled facility. *Journal of Intelligent & Robotic Systems*, pages 1–13, 2020.
- [24] *DJI E305 motor*.
<https://www.dji.com/it/e305/download>.
- [25] Robert C Nelson et al. *Flight stability and automatic control*, volume 2. WCB/McGraw Hill New York, 1998.

- [26] Grzegorz Szafranski and Roman Czyba. Different approaches of pid control uav type quadrotor. 2011.